OBSERVATION OF QUASI TWO-BODY PRODUCTION IN PION PLUS PROTON GOES TO NEUTRON PLUS FOUR CHARGED PIONS AT 8 GeV/c

BY

WILLIAM THADDEUS WROBLICKA

B.S., Cornell University, 1974
M.S., University of Illinois, 1975

THESIS

Submitted in partial fulfillment of the requirements
for the degree of Doctor of Philosophy in Physics
in the Graduate College of the
University of Illinois at Urbana-Champaign, 1980

Urbana, Illinois

DISCLAIMER

OBSERVATION OF QUASI TWO-BODY PRODUCTION IN PION PLUS PROTON GOES TO NEUTRON PLUS FOUR CHARGED PIONS AT 8 GeV/c

William Thaddeus Wroblicka, Ph.D.
Department of Physics
University of Illinois at Urbana-Champaign, 1980

This thesis reports the first observation of quasi 2-body production in the backward reaction $\pi^- p \to n\pi^+\pi^+\pi^-\pi^-$. Data were obtained using an 8 GeV/c pion beam incident on a liquid hydrogen target inside the University of Illinois/Argonne National Laboratory streamer chamber. The chamber was triggered by the interaction of a fast, forward neutral hadron in thick plate optical spark chambers. Total backward cross sections are derived for the processes $\pi^- p \to N^{*0}(1520)+\rho^0/f^0$, $N^{*0}(1670)+\rho^0/f^0$, $\Delta^0(1890)+\rho^0/f^0$, and $\Delta^-(1236)+A_2^+$. Evidence for a narrow A_1^+ resonance is not seen. Corrections for losses due to finite acceptance are made using Monte Carlo techniques based on a simple baryon exchange model. Comparison is made to another experiment regarding the energy dependence of certain cross sections and a simple power law behavior is observed.

ACKNOWLEDGEMENTS

The author gratefully acknowledges the advice and guidance of Drs. Ron Morris and Bob Wagner, from which he profited during his first years as a graduate student. More recently, Dr. Jim Elliott contributed greatly to the author's understanding of the data upon which this thesis is based, and to his appreciation of physics in general.

Most especially, though, the author thanks Professor Bob Eisenstein for his excellence as a teacher, advisor -- and friend.

This work was supported by the Department of Energy under contract EY-76-C-02-1195.

TABLE OF CONTENTS

1. Introduction

This thesis presents an analysis of the backward reaction

$$\pi^- p \rightarrow n\pi^+\pi^+\pi^-\pi^- \qquad 1\text{-}1$$

at 8 GeV/c, with particular regard to quasi 2-body (Q2B) intermediate states. Events of the type 1-1 represent a subset of the data gathered in an experiment to study the reaction

$$\pi^- p \rightarrow nX^0, \qquad 1\text{-}2$$

where X^0 represents any nonstrange system with net charge and baryon number zero. The experiment was performed at the Argonne National Laboratory Zero Gradient Synchrotron (ZGS) with the University of Illinois/Argonne National Laboratory streamer chamber facility.

A relatively large amount of data has been collected for backward elastic pion-nucleon scattering and for the backward inelastic charge exchange reaction $\pi^- p \rightarrow n\pi^0$ at energies greater than 4 GeV. A Reggeized baryon exchange model [see Barger (1969)] has been successful, at least qualitatively, in describing the energy dependence of cross sections, the shrinkage of the backward peak with increasing energy, and the occurrence of dips in the differential cross section at wrong signature, nonsense values of trajectories.

It is found that Q2B production accounts for a large fraction of backward inelastic cross sections in reactions with a final state multiplicity greater than two. To determine the extent that such data conform to a particular baryon exchange model is an important goal in the study of backward reactions.

Three body final states of the type $(n\pi^+\pi^-)$ and $(p\pi^-\pi^0)$ have been most extensively treated. Recent results include the observation of the backward production of the ρ^0, f^0, $\Delta^{\pm}(1236)$ [Eisenstein (1978), Arenton (1978)], and ρ^- [Benkheiri (1977), Scharre (1978)]. In all cases, consistency with

an N_α/Δ_δ exchange mechanism has been found. Fewer data are available for 4- and 5-body final states. Analysis becomes more difficult because of the lower q-value for such reactions and the appearance of identical particles in the final state.

This is the first experiment to observe Q2B production in the final state 1-1. It is found to account for approximately 30% of the 749 events selected for study. Total backward cross sections are derived for the processes

$$\begin{aligned} \pi^- p \rightarrow\ & N^{*0}(1520) + \rho^0/f^0, \\ & N^{*0}(1670) + \rho^0/f^0, \\ & \Delta^0(1890) + \rho^0/f^0, \\ & \Delta^-(1236) + A_2^+ . \end{aligned}$$

Evidence for a narrow A_1^+ resonance is not seen. Corrections for losses due to finite acceptance are made using Monte Carlo techniques based on a simple baryon exchange model for which consistency with certain features of the data is demonstrated. A comparison to previously published data is made regarding the energy dependence of the total backward cross section for the processes $\pi^- p \rightarrow N^{*0}(1520)+\rho^0/f^0$.

2. Data Acquisition

The reaction 1-2 is characterized by a neutron that is fast and forward in the laboratory ($\vec{p}^{L}_{n} \approx \vec{p}^{L}_{beam}$) and by a production cross section that is several orders of magnitude less than that of the corresponding forward process. This latter attribute dictates the need for a selective trigger, the source of which is the interaction of the neutron in a set of thick steel plate optical spark chambers.

The spark chambers and the streamer chamber comprise the principal elements of experimental hardware. The streamer chamber is well suited for the study of reaction 1-1 because it is triggerable and has multiple charged track detection ability. A detailed description of the streamer chamber's design and operation is available from Abashian (1974) and from Sokolsky (1973). Other components of experimental apparatus, its configuration, and the running conditions are identical to those discussed and cited by Eisenstein (1978). For completeness, however, a résumé is given here.

2.1 Apparatus

An elevation view (not to scale) of the experimental layout is shown in figure 2.1-1. Data for reaction 1-2 were gathered in two runs, between which improvements were made on the target and several counters were added to increase the event yield and reduce background. Figure 2.1-1 corresponds to the configuration for the second run.

2.1.1 Beam

The beam, nominally negative pions, was formed by the interaction of 12.5 GeV/c protons in a production target and was transported to the experimental region by a system of bending and focusing magnets. Contamination of the beam by muons, kaons, and antiprotons was estimated to be $\sim$6%. Three sets of x-y multiwire proportional chambers (MWPC's) served to define the beam angles. This information was unobtainable for approximately 20% of the events due to inefficiencies and ambiguities in the MWPC's.

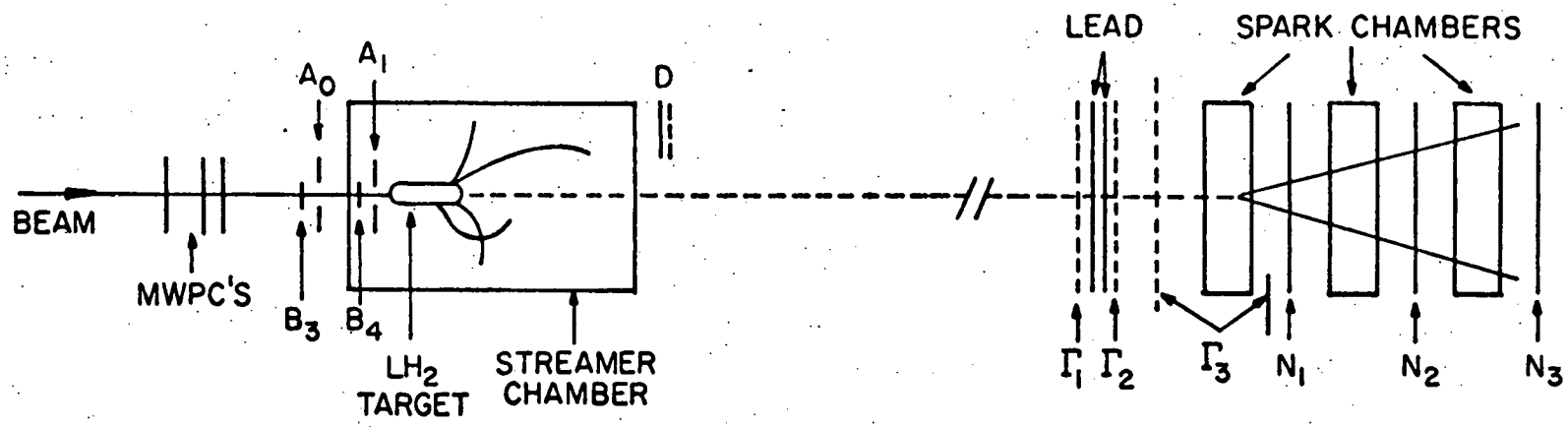

Figure 2.1-1 Elevation view (not to scale) of experimental layout.

In these cases average values for the beam angles were used. A beam intensity of $\sim 2\times10^5$ particles per ZGS spill was dictated by the 3 μs streamer chamber memory time, the 600 ms ZGS spill width, and the desire to avoid multiple beam tracks in streamer chamber photographs. The average beam momentum, calculated from photographs of noninteracting beam tracks, was 7.93 GeV/c for the first run and 8.04 GeV/c for the second run.

2.1.2 Target

A liquid hydrogen (LH_2) target was situated near the upstream end of the streamer chamber. It consisted of a cylindrical mylar flask 30.5 cm long, 3.8 cm in diameter, and was maintained at a temperature of 17.8° K. For thermal and electrical insulation, the flask was enclosed in a rectangular, opaque PVC-foam box. Consequently the event interaction vertex was invisible and was reconstructed by extrapolating measured charged particle tracks back into the target box.

2.1.3 Streamer Chamber

The chamber had a sensitive volume of $1.5\times1.0\times0.6$ m^3. It was filled with a 90% Ne/10% He gaseous mixture, plus a small amount of SF_6, an electronegative gas, to regulate memory time. The chamber was located within a large magnet with a 14.5 kG central field, so directed that negative beam particles were deflected upward. Photographs of charged particle tracks, which included $\sim$20 cm of the beam track, were taken in 18° stereo by three cameras positioned $\sim$2 m from the center of the chamber.

2.1.4 Spark Chambers

Each of the three chambers was filled with a 90% Ne/10% He gaseous mixture and consisted of a series of 21 $92.5\times122.5\times0.31$ cm^3 rectangular plates separated by a 0.95 cm gap. Sparks in the gaps delineated the trajectories of charged particles from a neutron interaction in one of the plates. The sparks were photographed in 90° stereo by a single camera through a system of mirrors. From the photographs the interaction vertex was reconstructed in space to within ±1.5 cm.

To reduce the number of interactions at the extreme front

and rear of each chamber, for which it was difficult to accurately reconstruct the vertex position, the first and last few plates were aluminum; the rest were stainless steel, for a total of one nuclear absorption length of material.

The transverse orientation of the spark chamber system with respect to the LH_2 target was such that a neutron produced at 0° relative to the beam would pass through the centers of the chambers. The distance from the LH_2 target to the spark chamber system was $\sim$11.5 m, fixed by the requirement that it be as small as possible without having noninteracting beam particles penetrate the chambers. From this distance and the neutron interaction position, the laboratory production angle of the neutron could be determined, the maximum being $\sim$3° relative to the beam.

2.1.5 Counters

Positioned upstream of the LH_2 target were two sets of counters, labeled A_0,B_3 and A_1,B_4 in figure 2.1-1, that signaled the beam-on-target condition. A_0 and A_1 were rectangular in shape with a 3.2 cm diameter hole in their centers. B_3 and B_4, with transverse dimensions 3.8×2.5 cm^2, were located in front of the holes so that a beam particle passing through the B counters and the holes would penetrate the target. A noninteracting beam particle, deflected upward by the streamer chamber's magnetic field, would strike a hodoscope array, labeled D. A beam interaction was thus defined by the logical condition $B_3 \cdot \bar{A}_0 \cdot B_4 \cdot \bar{A}_1 \cdot \bar{D}$.

Immediately behind each spark chamber was a plane of counters, labeled N_1,N_2,N_3 in figure 2.1-1. These were intended to detect charged secondaries resulting from neutron interactions in the chambers. Each plane consisted of four slightly overlapping counters with dimensions $91.5\times35.6\times0.95$ cm^3 covering the transverse area of the spark chambers.

The event trigger depends on the time lapse between a beam interaction and a neutron interaction. To minimize the uncertainty in the time of the latter, phototubes were attached to both ends of each spark chamber counter with a coincident signal requirement that precluded triggering on tube noise.

Most of the charged particles incident on the spark chamber system were detected by an array of counters, labeled Γ_1, Γ_2, Γ_3, in front of the system and $\sim$8.5 m from the LH_2 target. Incident photons were converted in 5.1 radiation lengths of lead sandwiched between Γ_1 and Γ_2. It was necessary to place another counter below the first spark chamber to detect charged particles resulting from interactions in the chamber support structure.

2.2 Trigger

A neutron interaction was defined by a signal from two out of three of the N counter planes in anticoincidence with a signal from any of the Γ counters. The two-out-of-three majority requirement was necessary to reduce spurious triggers.

To discriminate between slow neutrons from forward interactions and relatively fast neutrons from backward interactions a time-or-flight technique was used. The kinematically allowed spread in times-of-flight of neutrons from backward reactions of interest was $\sim$4 ns. Adding 3.5 ns for light transit time in the spark chamber counters and 2.5 ns for timing uncertainty defined a minimum time-of-flight gate width of $\sim$10 ns for accepting neutrons. In fact, the gate width was set at 23 ns to avoid the possibility of timing too tightly. Only those neutrons from forward reactions where the recoiling X^0 mass was near the kinematic limit ($\sim$3.05 GeV/c^2) would fall within the open gate. This was expected to represent a small and identifiable background.

Background triggers occurred mostly from photons incident on the spark chambers that were not converted by the lead plates between counters Γ_1 and Γ_2. It was estimated that these triggers could account for at most 25% of the total. Strange particle contamination of the beam could result in a fast, forward K_L^0 meson that would also satisfy the time-of-flight requirement and contribute to the background.

The trigger rate for the final run was 18 per 10^5 incident beam particles. The data rate was $\sim$1200 photographs per hour, being limited by the streamer and spark chamber dead times. A

total of 420 000 photographs was taken of events of the type 1-2. In addition, 8000 photographs were taken with a trigger requiring a beam interaction only, and 18 500 photographs were taken triggering on $pp \rightarrow nX^{++}$. These latter two data sets were useful in determining the cross section normalization.

3. Data Reduction

3.1 Event Reconstruction

The 420 000 streamer chamber photographs were scanned to eliminate events with a charge imbalance and events not having all tracks and fiducial marks visible in at least two views. In the process, events were classified according to the number of charged tracks in the final state. Two other categories were made for noninteracting beam tracks and for events exhibiting a "vee" or kinked track. Unacceptable photographs were scanned a second time, whereupon the results of both scans were combined.

Spark chamber photographs corresponding to acceptable streamer chamber photographs were scanned to determine the number and nature of interaction vertices.

Table 3.1-1 summarizes the scanning results. The numbers are percentages of the total number of photographs scanned.

Table 3.1-1

Streamer Chamber Film		Spark Chamber Film	
2 tracks	28%	no vertex	25%
4 tracks	22%	unique vertex	47%
6 tracks	5%	multiple vertices	20%
beam track	9%	photon vertex	8%
kinked track or "vee"	2%		
unacceptable photographs	34%		

Those events for which the streamer chamber photograph was acceptable and for which the spark chamber photograph had at least one possible neutron interaction vertex were processed by DOLLY, the University of Illinois semiautomatic measuring machine. The resulting digitized information was used by the standard program TVGP to reconstruct the streamer chamber tracks in space. The neutron interaction vertex position was reconstructed independently.

Event characteristics not directly obtainable from film include the primary interaction vertex position within the target and the beam angles. The program VERTEX extrapolated tracks into the LH_2 target and calculated the vertex as the point such that the sum of the squares of the distances from the point to each track was a minimum. The program also used MWPC information to calculate the beam angles.

If no other neutral particles are present, the only kinematic quantity lacking at this stage is the magnitude of the neutron's momentum. The momentum could in principle be computed from the time-of-flight data used to form the trigger. In fact, the spread in times of flight of backward produced neutrons was smaller than the uncertainty due to light transit time in the spark chamber counters and to timing jitter. Therefore the neutron momentum was calculated from 4-momentum conservation as part of the kinematic fitting procedure (section 3.3).

3.2 Event Rejection

A total of 20 910 candidates for events of the type

$$\pi^- p \rightarrow n + (4 \text{ charged tracks}) \qquad 3.2\text{-}1$$

was scanned, measured, and successfully reconstructed. This figure includes the effects of three quality cuts made to remove poorly measured or poorly reconstructed events. The first cut eliminated events with spatially reconstructed tracks that, when projected back onto the film plane, deviated substantially from the measured points on film. The second cut eliminated events with tracks whose kinematic parameters had atypically large errors. The third cut removed events for which the beam interaction vertex was poorly reconstructed.

Two more cuts were made prior to kinematic fitting. A target fiducial volume cut eliminated events resulting from interactions upstream of the target or in the insulating material surrounding the LH_2 flask. A cut was made on the distance of closest approach of a track to the interaction vertex. A track for which this distance was much larger than that for any of the other three tracks could result from a large angle

scatter within the target or the material surrounding it, the decay of a secondary inside the target, or a previously unrejected poor measurement. These two cuts reduced the data sample to 17 205 events.

3.3 Kinematic Fitting

Three-constraint fits to the event type 3.2-1 were made with the program SQUAW. The fitting procedure was repeated for various final state mass hypotheses, including

(a) $n\pi^+\pi^+\pi^-\pi^-$
(b) $nK^+\pi^+K^-\pi^-$
(c) $np\pi^+\bar{p}\pi^-$
(d) $\bar{n}pp\pi^-\pi^-$
(e) $nK^+\pi^+\pi^-\pi^-$
(f) $n\pi^+\pi^+K^-\pi^-$.

The inability of the trigger to distinguish neutrons from neutral kaons motivated the following hypotheses:

(g) $K_L^0p\pi^+K^-\pi^-$
(h) $K_L^0K^+p\pi^-\pi^-$
(i) $K_L^0p\pi^+\pi^-\pi^-$.

A zero-constraint calculation was performed for the hypothesis

(j) $n\pi^+\pi^+\pi^-\pi^-\pi^0$.

Finally, a 4-constraint fit, in which the neutron information was ignored, was performed to

(k) $p\pi^+\pi^-\pi^-$.

Strangeness nonconserving states such as (e), (f), and (i) could result from kaon contamination of the beam or from the decay of an intermediate, neutral, strange particle within the target.

The missing-mass-squared distribution for events of the type 3.2-1 is shown in figure 3.3-1. For computational purposes the charged final state particles were assumed to be pions. A neutron signal atop a large, featureless background is evident. There were 1355 such events that fit to hypothesis

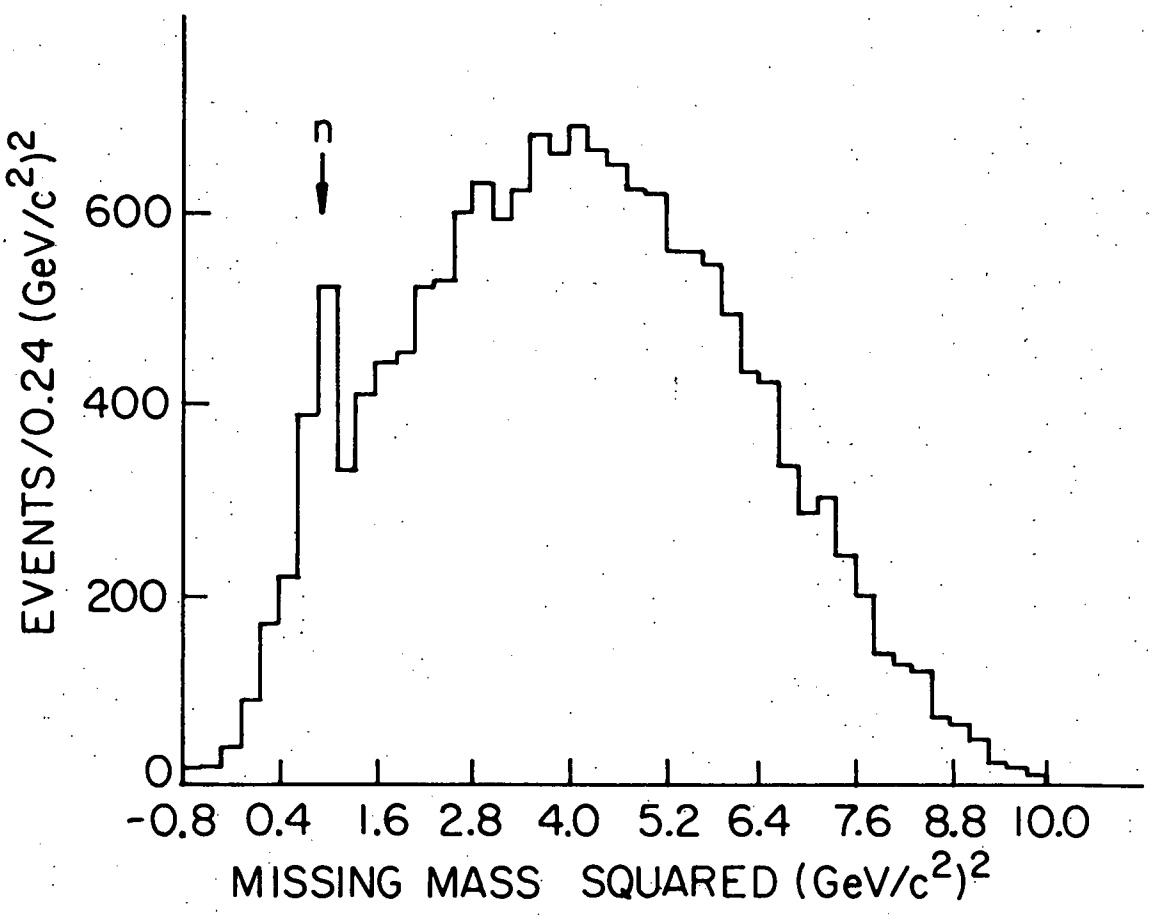

Figure 3.3-1 The missing-mass-squared distribution for events of the type $\pi^- p \to n +$ (4 charged tracks). The charged tracks are assumed to be pions for computational purposes.

(a) with a kinematic χ^2 less than 60. The missing-mass-squared distribution for these events is shown in figure 3.3-2. In the absence of contamination from other final states, the unshaded part of the plot would be symmetric about the neutron mass squared. The slight excess of events on the high mass side of the neutron peak is likely due to events of the type (j). In particular, the suggestive bump at 1.48 $(GeV/c^2)^2$ may indicate the $\Delta^0(1236)$ $(n\pi^0)$ resonance. The shaded region results from additional cuts described below.

There is a class of events for which one or more of the charged tracks are directed along the streamer chamber camera optic axis. These tracks, which tend to appear short and ill defined on film, were difficult to measure. Many such events are eliminated by the quality cuts described in section 3.2. Those remaining are removed by a cut on a track's angle with respect to the optic axis, decreasing the data sample by 21 events.

Figure 3.3-3 exhibits the relationship between the neutron momentum and the center of momentum angle between the neutron and the beam, θ_{bn}^{CM}. A momentum cut at 2 GeV/c removes all events in the forward region ($\cos\theta_{bn}^{CM} < 0$) and only 12 events in the backward region ($\cos\theta_{bn}^{CM} > 0$).

The kinematic χ^2 distribution for the remaining 1074 events is shown in figure 3.3-4. The solid curve is a fit to a theoretical χ^2 distribution with three degrees of freedom plus a constant term. The tail of the distribution includes many events that have been mistakenly classified as type (a). Of the type (a) events, 30% also fit to type (j), 43% fit to type (e), and 47% fit to type (f). This ambiguity cannot be attributed to poor measurement since these percentages are unaffected by the quality cuts.

Significant contamination from types (e) and (f) events with a charged kaon in the final state can be discounted for three reasons:

(1) The χ^2 distributions for all types (e) and (f)

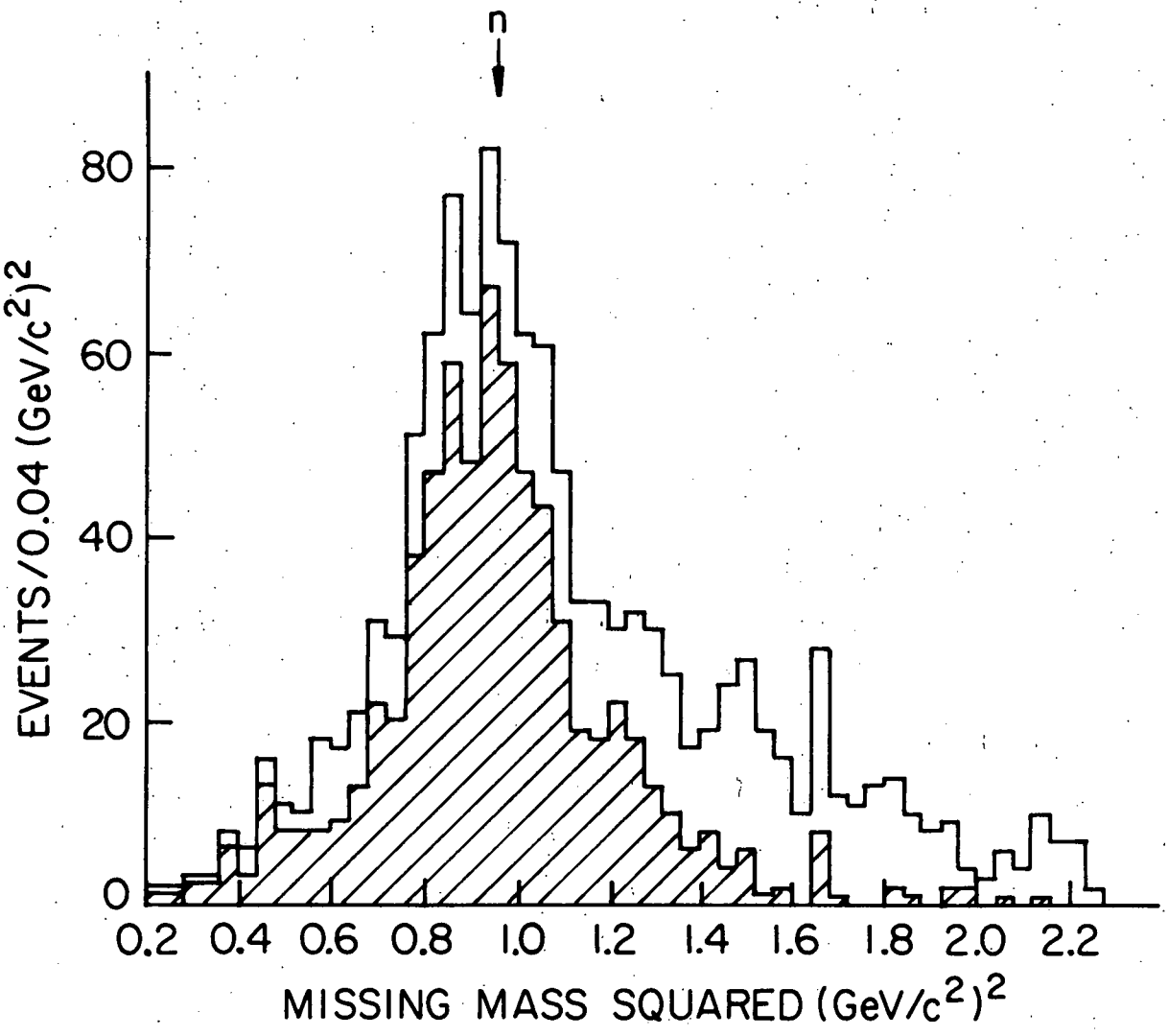

Figure 3.3-2 The missing-mass-squared distribution for events with a kinematic fit to the hypothesis $\pi^- p \to n\pi^+\pi^+\pi^-\pi^-$ before (unshaded) and after (shaded) the cuts described in the text are made.

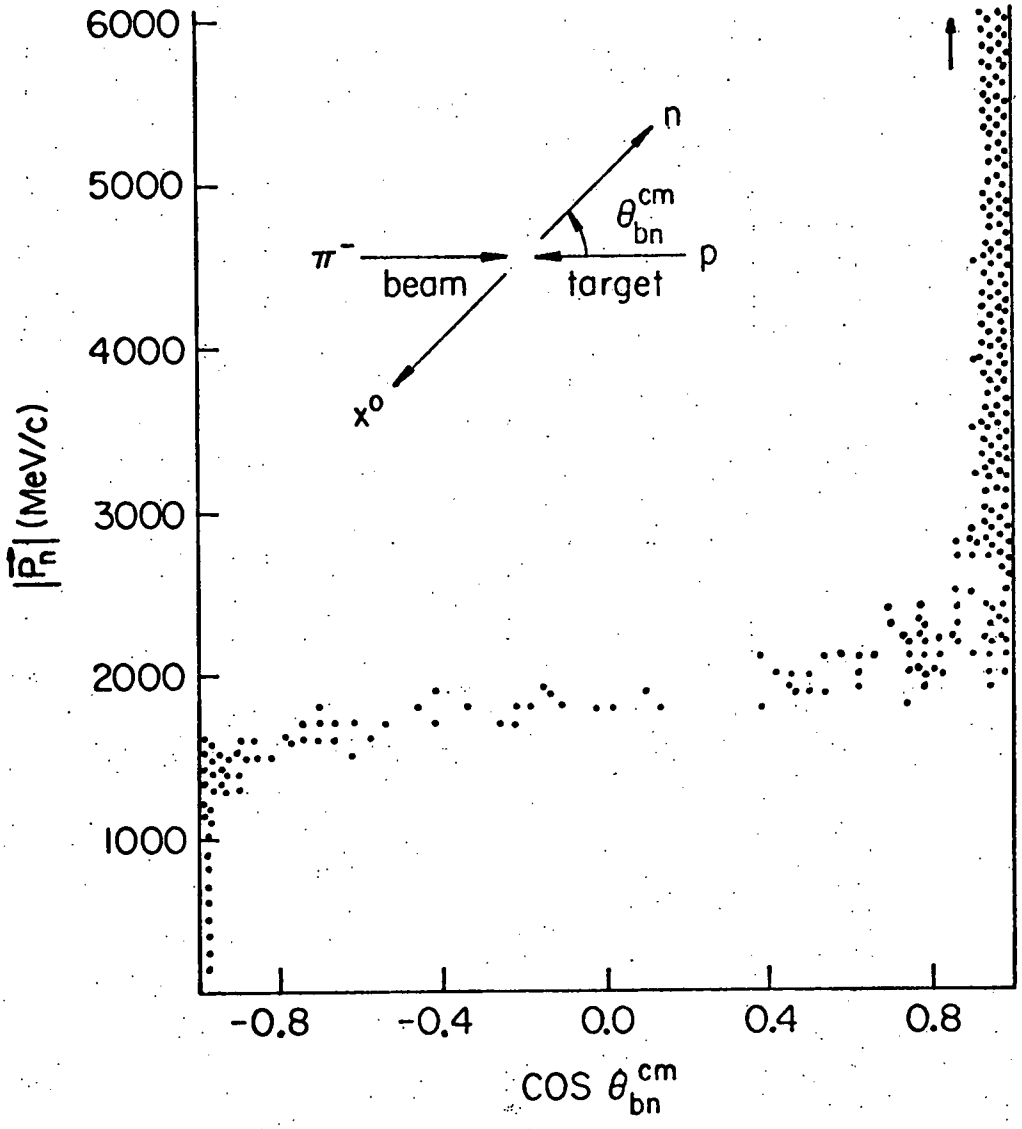

Figure 3.3-3 Scatterplot of the neutron laboratory momentum vs. the cosine of the center of momentum scattering angle between the neutron and the beam.

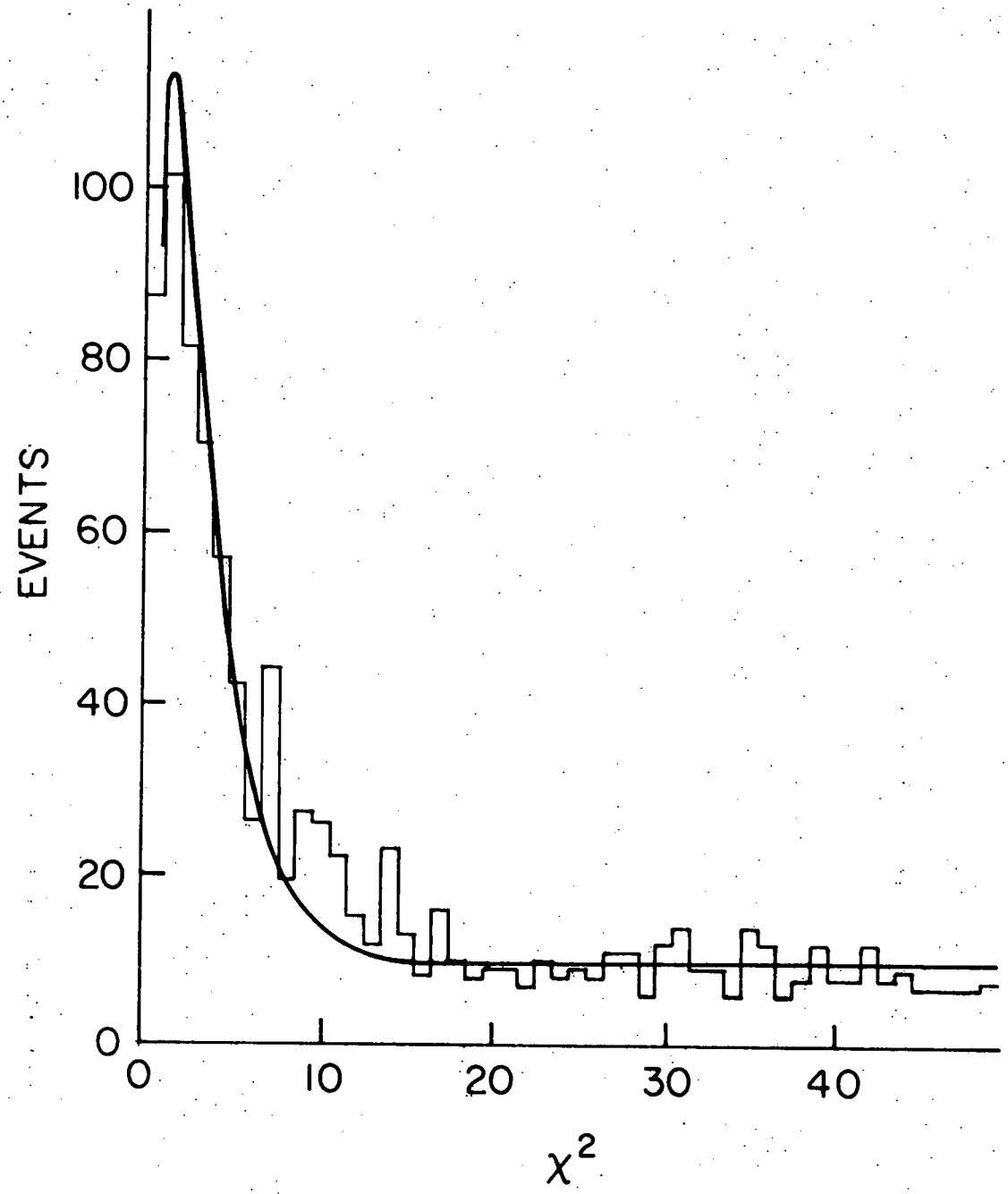

Figure 3.3-4 The kinematic χ^2 distribution of events with a fit to the hypothesis $\pi^- p \to n\pi^+\pi^+\pi^-\pi^-$. The solid curve is a fit to the data with a theoretical χ^2 distribution having three degrees of freedom, plus a constant term.

events show no peak characteristic of good fits.

(2) There is no evidence of resonance structure [e.g. $K^*(890)$] in the $K\pi$ or $K\pi\pi$ mass spectra.

(3) If strangeness conservation is invoked to associate a missing, neutral, strange particle with the single kaon in the final state, it is found that only $\sim$1% of types (e) and (f) events have a missing mass sufficiently large to allow for such a particle. For example, type (e) events would require a missing particle with baryon number 1, strangeness -1, and charge 0. The baryon with the lowest mass having these quantum numbers is the $\Lambda^0(1116)$, yet only 1.8% of type (e) events have a missing mass at least as large.

One concludes that the principal source of contamination in the type (a) event sample is events with an undetected π^0 in the final state.

To determine a reasonable point for making a χ^2 cut that will reduce this background and to estimate the number of type (a) events removed by the cut, it is necessary to gauge the efficiency of the kinematic fitting program. The procedure for doing so can be outlined as follows:

(1) Use a Monte Carlo technique to generate a set of type (a) events that conserve energy and momentum exactly. The tracks for such events are each parameterized by a mass and by a momentum vector, $\vec{p}_0$.

(2) Assign a measuring error, Γ^i, to the ith component of each track's momentum vector. Γ^i is selected at random from a Gaussian distribution whose mean and variance are characteristic of the real data.

(3) Generate a new momentum vector for each track by selecting the ith component at random from a Lorentzian distribution with mean p_0^i and width $2\Gamma^i$.

(4) Use these events as input to the fitting program.

The procedure was repeated for an equal number of type (j) events. Implicit here is the assumption that the production cross section is approximately the same for both types of events. Data compiled by Amaglobeli (1977) indicate this is true to within ∿15% at 5 GeV/c.

For a sample of Monte Carlo events that fit to hypothesis (a), the prediction is that 67% are legitimate and 33% are background. The result of the fit to the χ^2 distribution of figure 3.3-4 provides another estimate of the ratio of legitimate type (a) events to background as a function of χ^2. With a χ^2 cut at 21, the two estimates can be made self-consistent (equal). There remain 749 events, the missing-mass-squared distribution for which is shown in the shaded region of figure 3.3-2. This is the sample upon which the data analysis is based.

3.4 Cross Section Normalization

The proportionality constant that relates numbers of events of the type $\pi^- p \rightarrow n\pi^+\pi^+\pi^-\pi^-$ to a cross section is given by

$$\sigma_b = \frac{1}{n} \prod_i W_i, \qquad 3.4\text{-}1$$

where n is the nanobarn equivalent and the W_i are factors to correct for systematic losses of events. Table 3.4-1 lists the numerical values of the constants; there follows here a brief description of their meaning and derivation. For more detail, see Wagner (1978).

The nanobarn equivalent was calculated according to

$$n = \frac{A\rho}{m}\Phi N_t \lambda(1-e^{-\ell/\lambda})\times 10^{-33}, \qquad 3.4\text{-}2$$

where

A is Avogadro's number;

ρ is the density of hydrogen in the target;

m is the atomic weight of hydrogen;

Φ is the average beam flux incident on the target per trigger, corrected for beam contamination;

N_t is the number of triggers in the experiment;

ℓ is the average path length of a noninteracting beam particle in the hydrogen target; and

λ^{-1} is equal to $\lambda_I^{-1}+\lambda_D^{-1}$, with λ_I the mean interaction length of 8 GeV/c pions in hydrogen and λ_D the mean decay length of the beam.

For convenience, calculations for σ_b were based on a representative subset of the data. The factor W_1 scales the results according to the ratio of the number of 3-constraint fits in the subset to the number in the entire data sample.

W_2 scales the data in proportion to the number of events lost because they were unmeasured, poorly measured, or poorly reconstructed. It is given by the ratio of the number of events scanned, corrected for scanning accuracy and efficiency, to the number of events that remain after the three quality cuts are made on measured events.

W_3 accounts for events lost when the neutron interacts in the Γ counter-lead plate array upstream of the spark chambers.

W_4 corrects for events lost due to track scattering inside the target. The probability that a track scatters is proportional to the momentum dependent strong interaction total cross section and the reconstructed track length within the target. A worst-case assumption is made that every track scatter results in a lost event.

W_5 corrects for the small amount of streamer chamber film that was unscannable.

W_6 accounts for events lost when a neutron enters the spark chamber system but does not result in a trigger. The problem of determining the efficiency of the spark chamber system is discussed in the Appendix.

Finally, W_7 is a correction factor for the number of events lost in making the χ^2 cut, as well as the number of background events that remain after this cut is made. The correction is based on the results of the kinematic fitting efficiency analysis described in section 3.3.

The error in W_7, which dominates all others, was calculated on the basis of a worst-case assumption that the true number of background events in the sample prior to making the χ^2 cut is equally likely to be found within a range $N_0 \pm \delta$. Here the median value, N_0, is the best estimate of the number of background events, predicted by the kinematic fitting efficiency analysis. The upper limit, $N_0 + \delta$, is the number given by the fit to the χ^2 distribution in figure 3.3-4. It was decided to ignore this large systematic uncertainty in subsequent calculations of cross sections; it is therefore omitted from the absolute error on the cross section basis quoted below.

Table 3.4-1

A	6.02×10^{23}	atoms/mole
ρ	0.0734 ± 0.0003	g/cm^3
m	1.008	g/mole
Φ	5452 ± 91	pions/trigger
N	47 095	triggers
λ^t	814.2 ± 9.4	cm
ℓ	30.5 ± 0.1	cm
n	0.337 ± 0.008	events/nb
W_1	0.122	
W_2	3.25 ± 0.08	
W_3	1.25	
W_4	1.05 ± 0.01	
W_5	1.047 ± 0.002	
W_6	2.67 ± 0.36	
W_7	0.96 ± 0.19	
σ_b	4.13 ± 0.57 (not including an overall systematic uncertainty of 20%)	nb/even

4. Data Analysis

4.1 Introduction

In this chapter the 749 events that fit to the backward reaction hypothesis

$$\pi^- p \rightarrow n\pi^+\pi^+\pi^-\pi^- \qquad 4.1\text{-}1$$

will be examined for evidence of quasi 2-body (Q2B) final states. The term "backward" refers to a center-of-momentum (CM) scattering angle between the beam and the detected neutron of less than 90°. The term "Q2B" refers to a state in which the observed particles devolve from two intermediaries, as illustrated in figure 4.1-1.

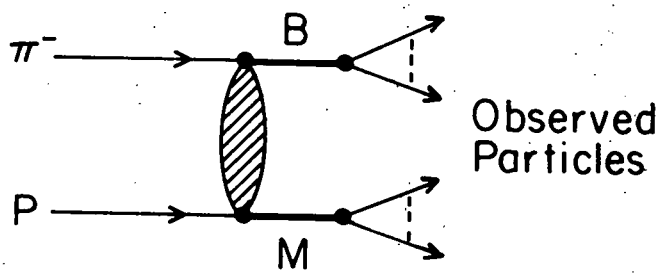

Figure 4.1-1 A Q2B event.

For backward πN reactions, one of the intermediaries (conventionally the one at the upper vertex) will have the quantum numbers of a baryon (B), while the other will have those of a meson (M). B and M may be either resonances or stable particles.

Published results are available for only three πN scattering experiments that measured a final state of the type (nucleon)+(charged pions) with a multiplicity sufficiently high to warrant a study of Q2B production. The observation of copious Q2B production in two of them motivates the search for such states in this data. Table 4.1-1 catalogues the states previously studied. The third experiment, reported by Arenton (1978), found no clear evidence for Q2B production.

Table 4.1-1

Reaction	Reference	Channel	Q2B States	Notes
$\pi^- p \to p\pi^-\pi^+\pi^-$ at 9 and 12 GeV/c	Ferrer (1978)	$(p\pi^-)(\pi^+\pi^-)$	$\Delta^0(1236) + \rho^0/f^0$	a
			$N^{*0}(1520) + \rho^0/f^0$	a
			$N^{*0}(1688) + \rho^0/f^0$	a
		$(p\pi^+\pi^-)(\pi^-)$	$N^{*+}(1520) + \pi^-$	a
			$N^{*+}(1670) + \pi^-$	b
			$\Delta^+(1890) + \pi^-$	a
		$(p\pi^-\pi^-)(\pi^+)$	$\Delta^-(1890) + \pi^+$	a
		$(p)(\pi^+\pi^-\pi^-)$	$A_2^- + p$	a
			$A_1^- + p$	a
$\pi^- p \to p\pi^-\pi^+\pi^-$ at 8 GeV/c	Abashian (1976) Morris (1975)	$(p\pi^-)(\pi^+\pi^-)$	$\Delta^0(1236) + \rho^0/f^0$	a
			$N^{*0}(1520) + \rho^0/f^0$	a
			$N^{*0}(1670) + \rho^0/f^0$	b
		$(p)(\pi^+\pi^-\pi^-)$	$A_2^- + p$	c
			$A_1^- + p$	c
			$S(1930) + p$	b

Notes

(a) This state considered clear and unambiguous in the data.

(b) A clear enhancement is seen in data, but its association with the given resonance is ambiguous.

(c) This state unclear but possible.

A feature common to most backward reactions at energies $\gtrsim$ 4 GeV is the peak in the differential cross section as $\theta_{bB}^{CM} \to 0°$, where θ_{bB}^{CM} is the CM scattering angle between the beam and the baryon. The gross shape of the peak is well parameterized by

$$\frac{d\sigma}{du_B'} = Ae^{-b|u_B'|}, \qquad 4.1\text{-}2$$

where

$$u_B' \equiv u_B(\theta_{bB}^{CM}) - u_B(0) = 2p_b^{CM} p_B^{CM} (\cos\theta_{bB}^{CM} - 1) \qquad 4.1\text{-}3$$

and u_B is the 4-momentum transfer between the beam and baryon. The fine structure of the peak, particularly its behavior when $\theta_{bB}^{CM} \simeq 0°$, bears on the phenomenology of Q2B production at fixed energy. It must be stated, however, that the lack of statistics, limited acceptance in θ_{bB}^{CM}, and the complexity of the final state 4.1-1 make it impossible to obtain a quantitative understanding of the production mechanism for Q2B states observed in this data.

On the contrary, in order to derive cross sections for Q2B production, it will be necessary to postulate a model, the simplest for which consistency with the data can be demonstrated. To this end, one assumes that the amplitude for the process $\pi^- p \to$ BM corresponds to the diagram sketched in figure 4.1-2.

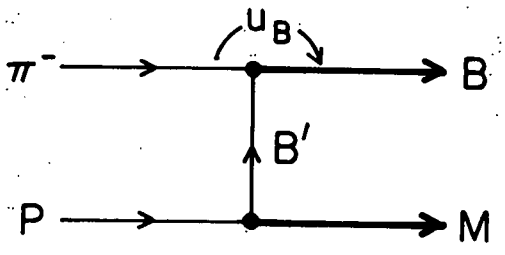

Figure 4.1-2 One particle (baryon) exchange picture.

The virtual baryon propagator, B', is assumed to have definite isospin and an angular momentum independent of u_B.

Support for this picture is provided by the results of the two experiments listed in table 4.1-1, which were found to be consistent with the exchange of a single, unpolarized baryon. Furthermore, when conservation rules allowed more than one possibility for the identity of the exchanged baryon, the one with the lowest mass appeared to dominate.

4.2 Overview of the Data

Table 4.1-1 suggests that the following possibilities for Q2B intermediaries in reaction 4.1-1 be investigated:

B	M
$(n\pi^+\pi^-)$	$(\pi^+\pi^-)$
$(n\pi^-)$	$(\pi^+\pi^+\pi^-)$
$(n\pi^+)$	$(\pi^+\pi^-\pi^-)$

The m_B vs. m_M invariant mass scatterplots corresponding to these channels were studied. In none of them was there significant clustering of events indicative of Q2B production. The projections, however, are not featureless. Figure 4.2-1(a) shows the $(n\pi^+\pi^-)$ mass distribution in which there is possible resonance structure near 1600 MeV/c^2. The $(\pi^+\pi^-)$ mass distribution in figure 4.2-1(b) shows a prominent ρ^0 signal and an enhancement in the region of the f^0 around 1270 MeV/c^2. In view of the preponderance of $N^{*0} + \rho^0/f^0$ Q2B production listed in table 4.1-1, this is encouraging. In figure 4.2-2(a) the $(n\pi^-)$ mass distribution evidently contains some $\Delta^-(1236)$, which is not accompanied by clear meson resonance structure in the $(\pi^+\pi^+\pi^-)$ mass distribution in figure 4.2-2(b). The $(n\pi^+)$ and $(\pi^+\pi^-\pi^-)$ mass distributions in figure 4.2-3 are devoid of structure in the neighborhood of known resonances.

It should be noted that no attempt has yet been made to discriminate among the final state pions. The distributions in figure 4.2-1, for example, contain four entries per event, one

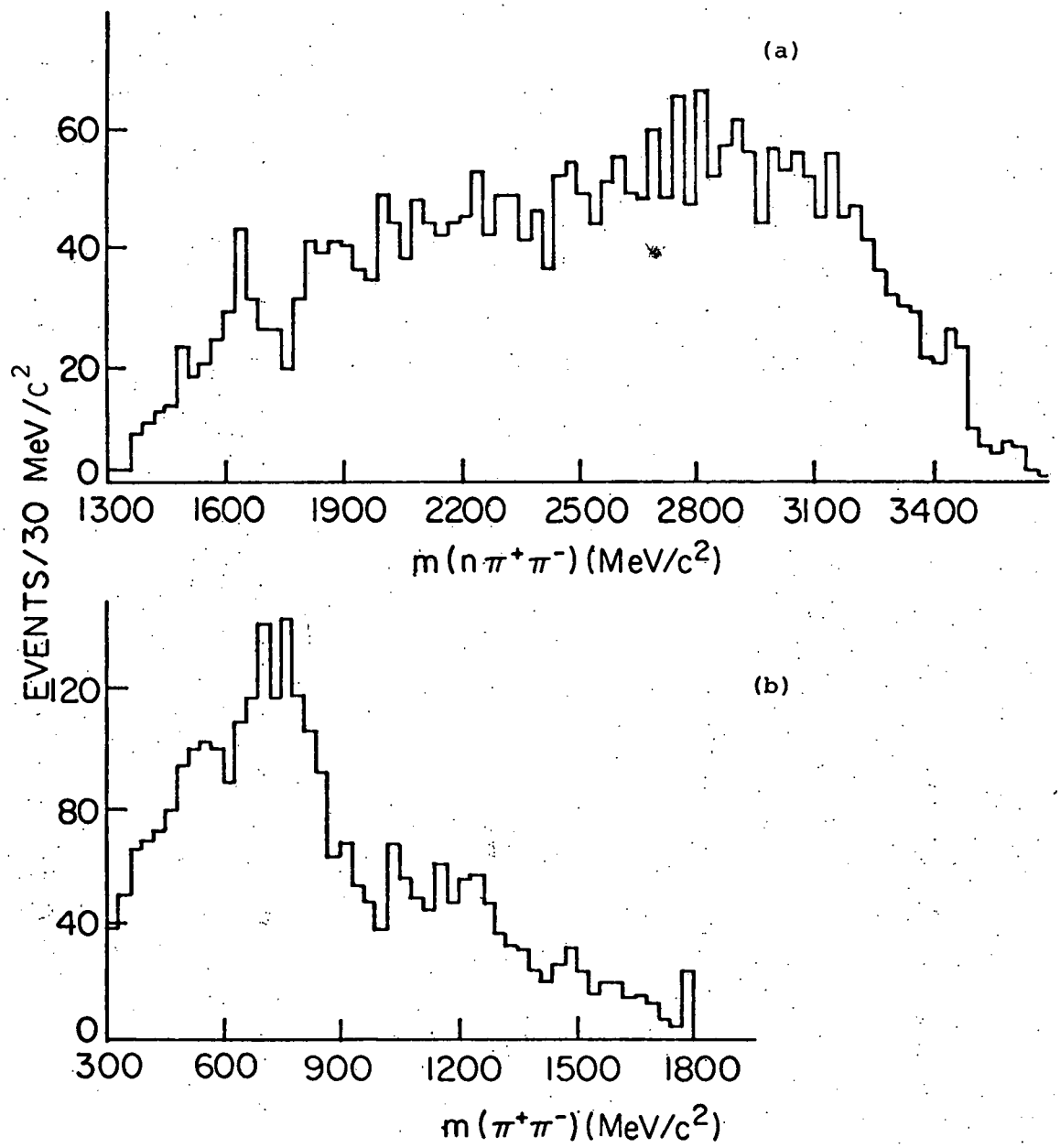

Figure 4.2-1 Invariant mass distributions, with four entries per event, of (a) the $(n\pi^+\pi^-)$ particle combinations and (b) the recoiling $(\pi^+\pi^-)$ particle combinations.

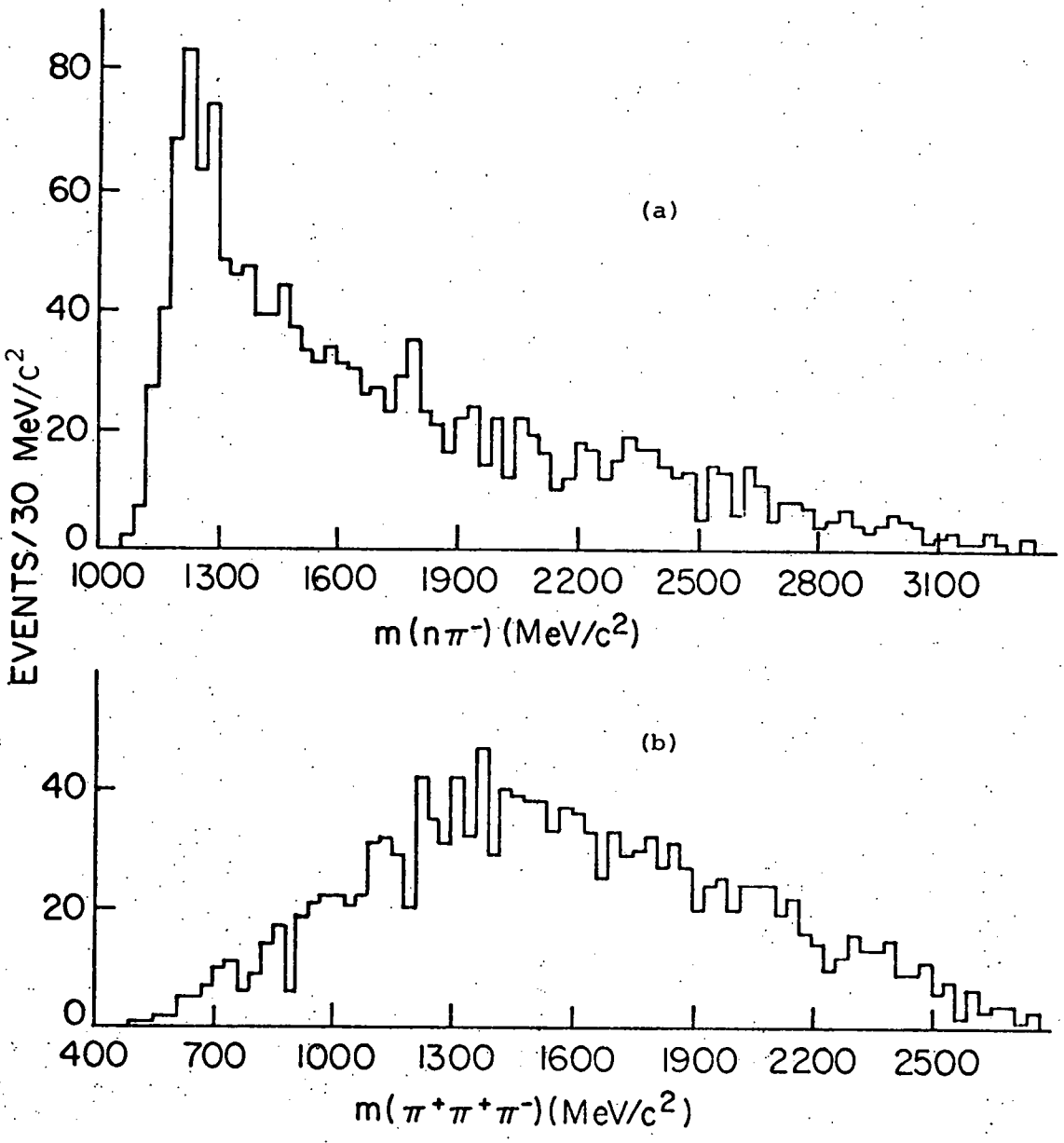

Figure 4.2-2 The invariant mass distributions, with two entries per event, of (a) the $(n\pi^-)$ particle combinations and (b) the recoiling $(\pi^+\pi^+\pi^-)$ particle combinations.

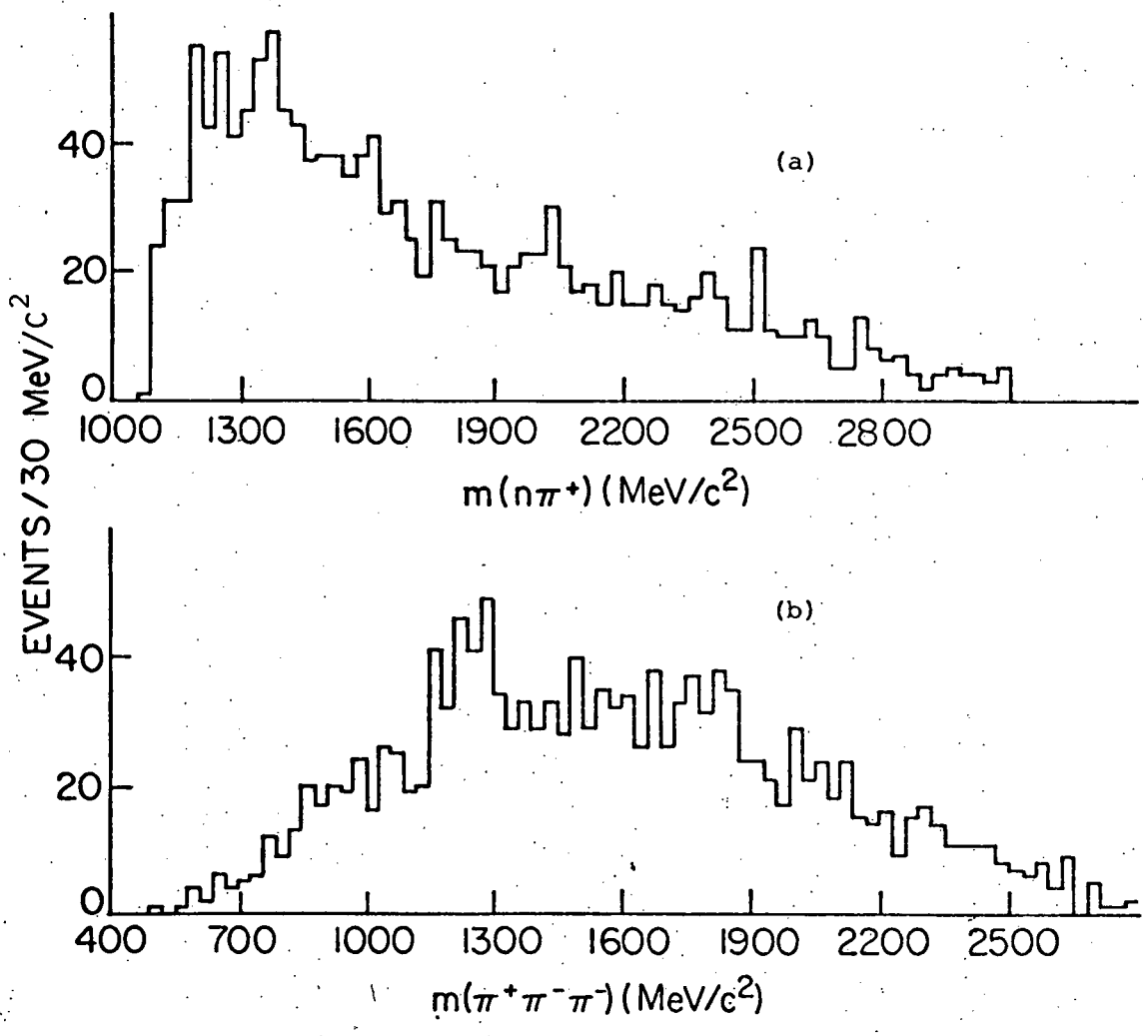

Figure 4.2-3 The invariant mass distributions, with two entries per event, of (a) the $(n\pi^+)$ particle combinations and (b) the recoiling $(\pi^+\pi^-\pi^-)$ particle combinations.

for each of the four possible ways to pair two pions with net charge zero. If every event in the data were Q2B, the signal to noise ratio in the figure would be only 1/3. It is undoubtedly smaller because of events in which none of the $(\pi^+\pi^-)$ pairs is resonant. A similar caveat applies to figures 4.2-2 and 4.2-3 for which there are two entries per event.

In summary, the data motivate a search for known low mass baryon resonances recoiling from ρ^0 or f^0 mesons, and known meson resonances recoiling from a $\Delta^-(1236)$.

4.3 The $(n\pi^+\pi^-)(\pi^+\pi^-)$ Channel

4.3.1 Pion Discrimination

In the laboratory (L) frame, the canonical backward Q2B reaction involves a baryon that is "fast" relative to the recoiling meson in the sense that $p_B^L > p_M^L$. If $\sqrt{s}$ were sufficiently large relative to both m_B and m_M, it would then be true that $p_{\pi_B}^L > p_{\pi_M}^L$, where π_B (π_M) is a pion from the decay of the baryon (meson). In this experiment, however, it is possible for $p_{\pi_B}^L \lesssim p_{\pi_M}^L$, particularly when $\theta_{b\pi_B}^{CM} \simeq 180°$ and $\theta_{b\pi_M}^{CM} \simeq 0°$, making the parentage of the pions ambiguous. This overlap in momenta (and in momentum dependent functions) worsens as the resonance masses increase. In the discussion that follows, the term "misassociation" will refer to a pion resulting from the decay of the baryon (meson) resonance that is mistakenly associated with the meson (baryon) resonance.

For the $(n\pi^+\pi^-)(\pi^+\pi^-)$ channel, pion discrimination is accomplished by a method less straightforward than simple momentum ordering. The pion pair associated with the meson [baryon] resonance will be labeled $(\pi_1^+\pi_2^-)$ $[(\pi_3^+\pi_4^-)]$, with π_1^+ and π_2^- chosen so that $|u'_{(n\pi_1^+\pi_2^-)}|$ is the largest of the four possibilities. This scheme can be heuristically explained as follows: According to equation 4.1-2, $|u'_B| = |u'_{(n\pi_3^+\pi_4^-)}|$ is likely to be small. For a misassociation involving one pion, the kinematic ambiguity mentioned above may cause $|u'_{(n\pi_1^+\pi_4^-)}|$ or $|u'_{(n\pi_3^+\pi_2^-)}|$ to be at least as small. It is unlikely, however, that a misas-

sociation involving two pions will yield a value of $|u'|$ smaller than $|u'_B|$; i.e., it is unlikely that $|u'_{(n\pi^+_1\pi^-_2)}| < |u'_{(n\pi^+_3\pi^-_4)}|$. Monte Carlo studies support this assertion. See section 4.3.5.

4.3.2 Evidence for Q2B Production

The prescription described above was applied to the data. Figure 4.3.2-1 exhibits the $(n\pi^+_3\pi^-_4)$ mass distribution. At the low mass end (below 1960 MeV/c^2), where the pion association scheme is expected to be most reliable and where other experiments have seen considerable resonance production, structure is visible in three regions (henceforth, regions 1, 2, and 3) centered at 1520, 1640, and 1840 MeV/c^2.

The recoiling $(\pi^+_1\pi^-_2)$ distribution is shown in figure 4.3.2-2. The ρ^0 signal is clear, and there is better evidence of an f^0 signal. Those events for which $m_{(n\pi^+_3\pi^-_4)} < 1960$ MeV/c^2 are contained in the shaded area. The result of this cut is an improved ρ^0 signal in that the low mass shoulder has been reduced. The f^0 signal is relatively unaffected by the cut. Unless otherwise noted, the discussion that follows in this section refers to the 347 events that remain after this mass cut is made.

Despite the small number of events, evidence for Q2B production can be seen in figure 4.3.2-3, a scatterplot of $m_{(\pi^+_1\pi^-_2)}$ vs. $m_{(n\pi^+_3\pi^-_4)}$ for $m_{(n\pi^+_3\pi^-_4)} < 1960$ MeV/c^2. There is a well-defined ρ^0 band with indications of clustering in regions 1 and 2 combined and in region 3. The events associated with the f^0, being so few, are difficult to resolve into clusters.

The density of events on the low side of the ρ^0 band appears to increase with increasing $m_{(n\pi^+_3\pi^-_4)}$. Most of these events can be attributed to pion misassociation, for, as figure 4.3.2-4 shows, the $(\pi^+_3\pi^-_4)$ pairs associated with the baryon are distributed smoothly in mass around 550 MeV/c^2. An empirical estimate of the number of such events puts it at $\sim$10% of the total.

The accumulation of events between the ρ^0 and f^0 seen in

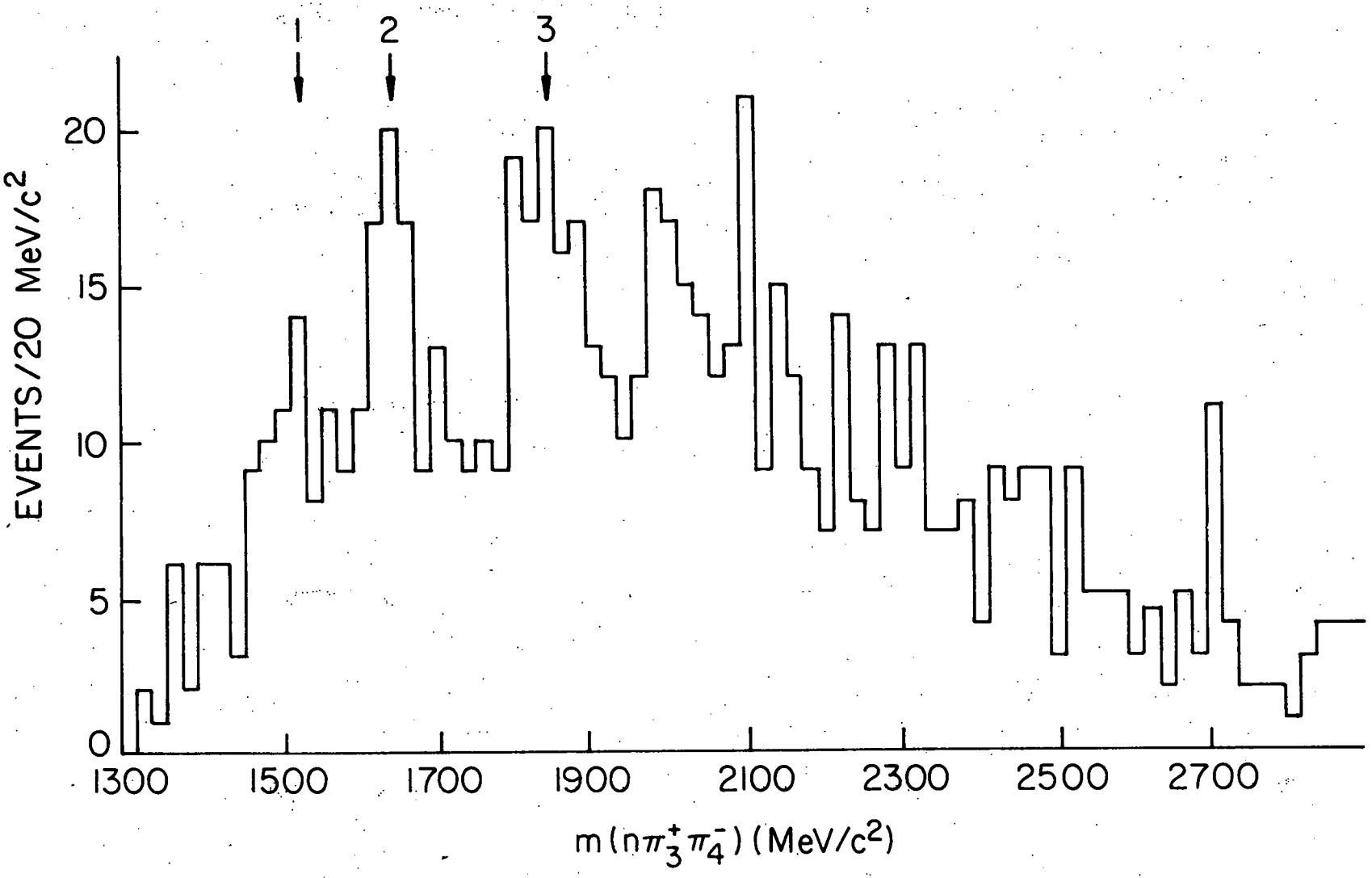

Figure 4.3.2-1 The invariant mass distribution of the particle combination associated with the-baryon showing possible resonance structure in three regions.

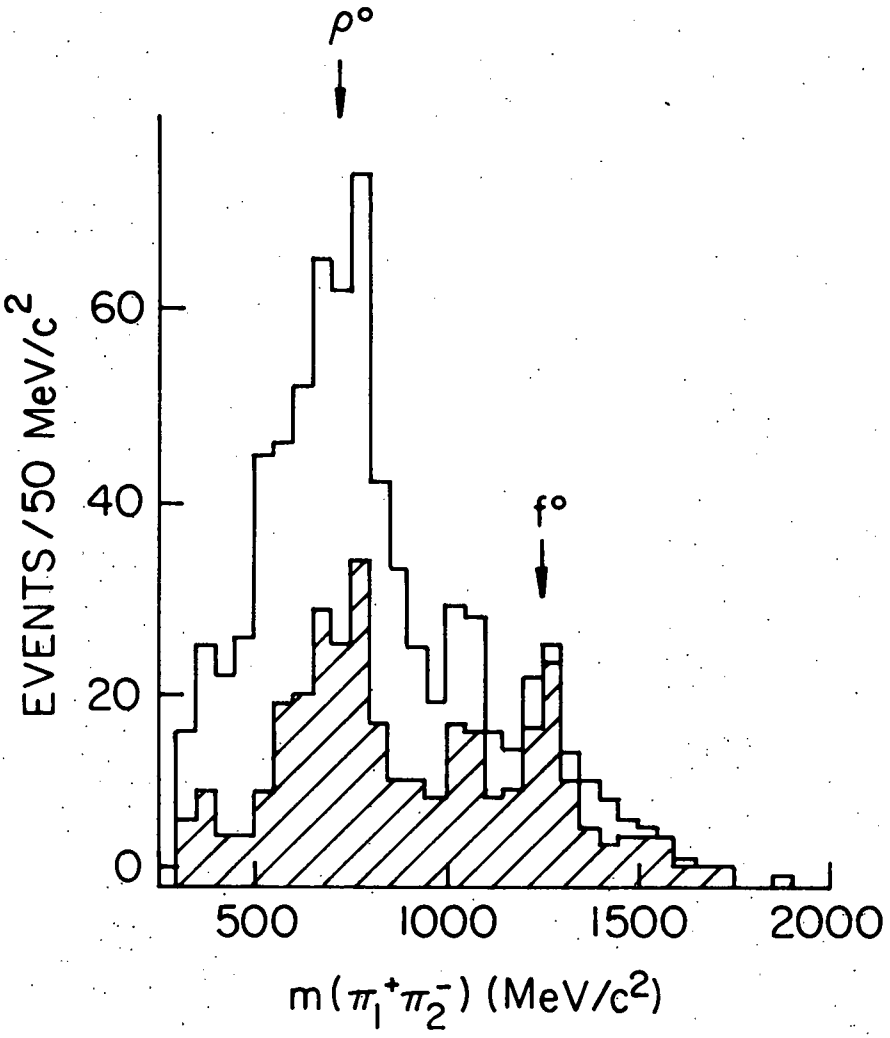

Figure 4.3.2-2 The invariant mass distribution of the pion pair associated with the meson showing a ρ^0 signal and a possible f^0 signal. The shaded area contains events for which $m_{(n\pi_3^+\pi_4^-)} < 1960$ MeV/c^2.

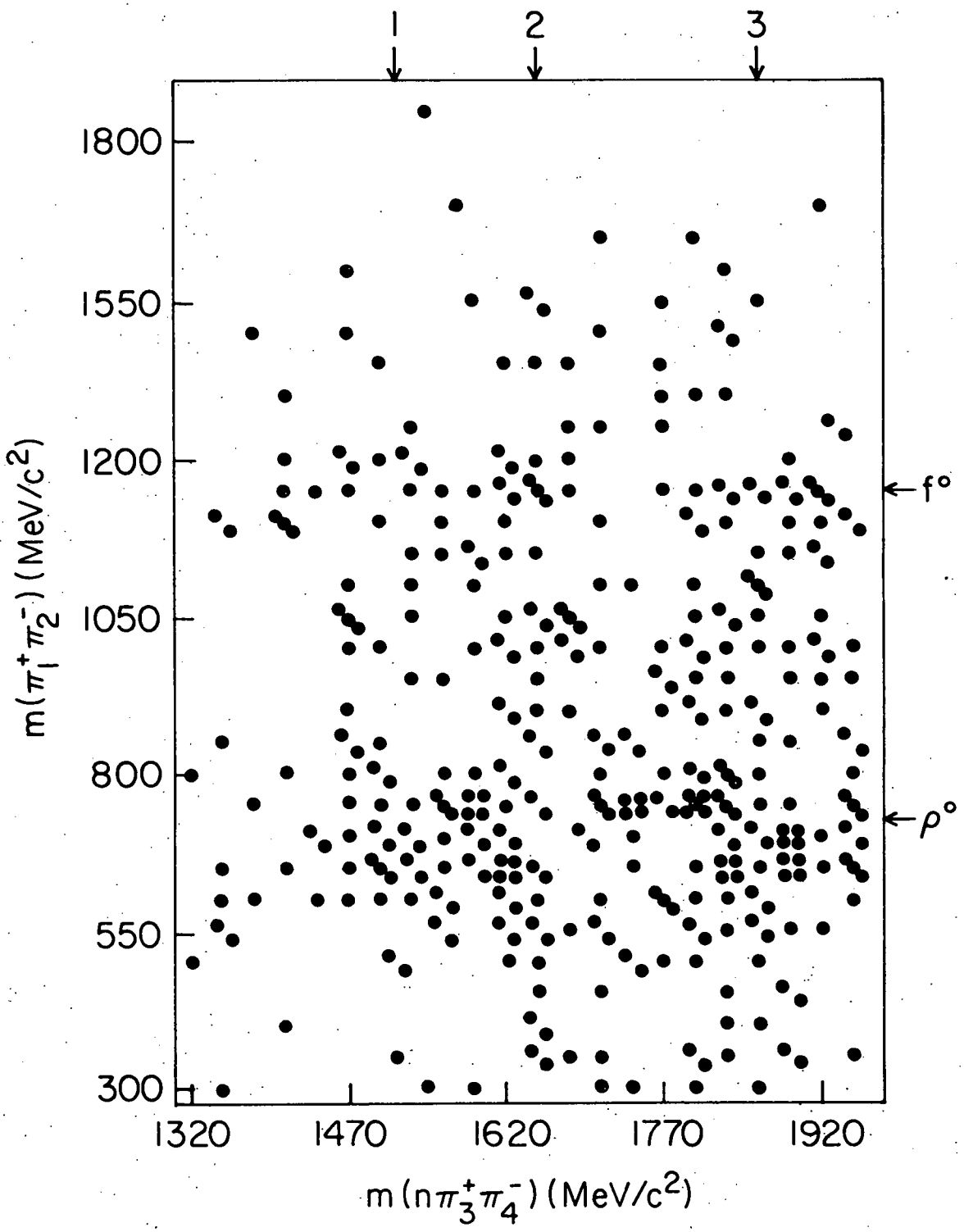

Figure 4.3.2-3 The invariant mass scatterplot of the meson particle combination vs. the baryon particle combination. Bands of possibly resonant events are indicated.

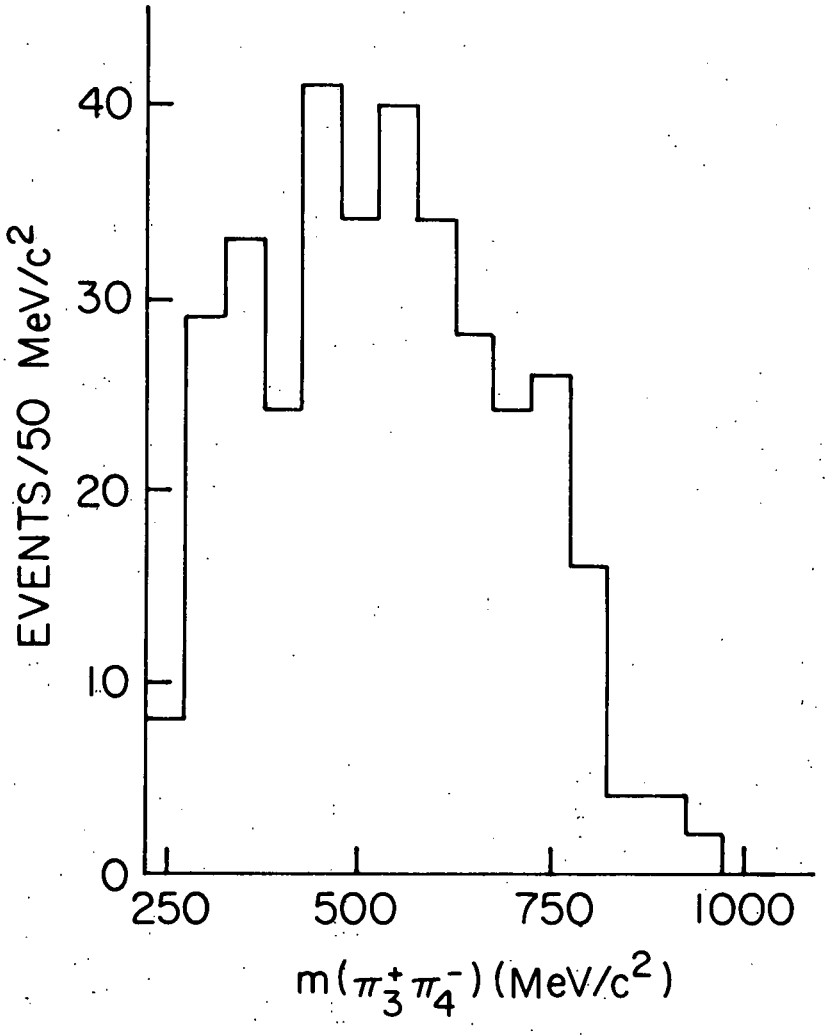

Figure 4.3.2-4 The invariant mass distribution of the pion pair associated with the baryon particle combination.

figure 4.3.2-2 appears in figure 4.3.2-3 to form a cluster in regions 2 and 3. It is unlikely this enhancement is a mere statistical fluctuation as similar structure has been reported by Abashian (1976). There is some evidence, reviewed by Bricman (1978), from phase shift analyses of $\pi\pi$ elastic scattering for a narrow $I(J^P) = 0(0^+)$ s-wave resonance, the S^*, in this mass region. The data here do not permit statistically significant conclusions to be drawn regarding the backward production of this state.

4.3.3 Fits to the Data

Least Squares fits to both the $(n\pi_3^+\pi_4^-)$ and $(\pi_1^+\pi_2^-)$ mass distributions were performed. The results are listed in table 4.3.3-1.

Table 4.3.3-1

Baryon Resonance	Mass (MeV/c^2)	Width (MeV)	No. of Events
1	1518±12	125 (fixed)	78±15
2	1649± 7	65±22	76±21
3	1860±11	182±41	179±21
	Confidence Level 95%		
Meson Resonance			
ρ^0	732±19	155 (fixed)	145±17
f^0	1254±15	180 (fixed)	74±17
	Confidence Level 46%		

The fitting function had the general form

$$f(m) = \sum_{i=1}^{n_R} \frac{\beta_i}{(m-m_i)^2+(\frac{1}{2}\Gamma_i)^2} + \text{background.} \qquad 4.3.3\text{-}1$$

One nonrelativistic Breit-Wigner function was included for each resonance in the distribution. Neither the fitted parameter values nor the χ^2 values for the fits were sensitive to such refinements as the use of relativistic Breit-Wigner func-

tions with mass dependent widths.

A background function of the form $\Sigma_{i=0}^{2}\alpha_i(m-m_0)^i$, where m_0 is the threshold mass, was found to be both necessary and sufficient to describe the $(\pi_1^+\pi_2^-)$ distribution. That is, the distribution was not well fit with two Breit-Wigner functions alone, while the confidence level for the fit was not improved with the inclusion of more terms in the background function. The contribution to the fit from events with 1000 MeV/c^2 < $m_{(\pi_1^+\pi_2^-)}$ < 1100 MeV/c^2 (the S*-region) was ignored.

Unlike the meson resonance parameters, those for the baryon resonances were strongly influenced by the choice of a background function. With the mass cut at 1960 MeV/c^2, however, the $(n\pi_3^+\pi_4^-)$ distribution was well fit by three Breit-Wigner functions alone. Contamination from pion misassociation is expected to be minimal in region 1 but to increase with increasing mass. The numbers of events, therefore, particularly for region 3, should be interpreted as upper limits; the errors do not reflect systematic effects of fitting.

The number of events associated with each resonance was computed by integrating the Breit-Wigner function over the mass range of the entire distribution. The errors quoted in table 4.3.3-1 are statistical only.

The number of Q2B events was obtained by performing a two-dimensional fit to the data in figure 4.3.2-3. Because the density of events is so low, the Least Squares method is not applicable. Instead, a Maximum Likelihood fit was done whereby the joint probability density function

$$F(\vec{\alpha}) = -\sum_{i=1}^{N} \ln[P(m_B^i, m_M^i; \vec{\alpha})] \qquad 4.3.3\text{-}2$$

was minimized with respect to the parameter array, $\vec{\alpha}$. Here N is the total number of events in the scatterplot, and m_B^i and m_M^i are the masses for the ith event that define a point in the plot.

The function P is simply the product of the functions used to fit the projected distributions (see equation 4.3.3-1):

$$P(m_B^i, m_M^i; \vec{\alpha}) = \sum_{j=1}^{3} \sum_{k=1}^{2} w_l(\vec{\alpha}) \frac{\eta_l}{[(m_B^i-\mu_B^j)^2+(\tfrac{1}{2}\Gamma_B^j)^2][(m_M^i-\mu_M^k)^2+(\tfrac{1}{2}\Gamma_M^k)^2]}$$

$$+ \sum_{j=1}^{3} w_l(\vec{\alpha})\eta_l \frac{a_0+a_1(m_M^i-m_0)+a_2(m_M^i-m_0)^2}{(m_B^i-\mu_B^j)^2+(\tfrac{1}{2}\Gamma_B^j)^2}. \qquad 4.3.3\text{-}3$$

The nominal masses and widths, $\mu_B^j, \mu_M^k, \Gamma_B^j, \Gamma_M^k$, and the background constants, a_0, a_1, a_2, are taken from the fit results to the projected distributions. The normalization constants, η_l, $l=1,\ldots,9$, are fixed so that the integral of the lth term in P is equal to $w_l(\vec{\alpha})$, a normalized parameter:

$$w_l(\vec{\alpha}) = \frac{\alpha_l}{\Sigma_{i=1}^{9}\alpha_i}. \qquad 4.3.3\text{-}4$$

The number of events associated with a term in equation 4.3.3-3 is given by

$$N_l = w_l N. \qquad 4.3.3\text{-}5$$

These numbers are listed in table 4.3.3-2.

Table 4.3.3-2

	ρ^0	f^0	background	Totals
Baryon Region				
1	47.5±6.6	30.5±7.3	9.7±10.7	87.7±14.5
2	19.1±3.5	10.1±2.8	45.8±12.1	75.0±12.9
3	68.3±9.0	29.1±8.3	86.1±15.6	183.5±19.8
Totals	134.9±11.7	69.7±11.4	141.6±22.4	

The totals above should and do agree, within errors, with the results of the independent fits to the projected distributions.

As another check of the goodness of the Maximum Likelihood fit, figure 4.3.2-3 was divided into a number of rectangular bins so that a χ^2 statistic could be defined:

$$\chi^2 = \sum_{i=1}^{b} \frac{1}{n_f^i} (n_o^i - n_f^i)^2, \qquad 4.3.3\text{-}6$$

where b is the number of bins, n_o^i is the number of events observed in the ith bin, and n_f^i is the number of events predicted by the fit in the ith bin, obtained by integrating equation 4.3.3-3 over the area of the bin. Using a technique described by Eadie (1971), one can construct a goodness-of-fit test based on this statistic. The boundaries of the bins were chosen to equalize the number of fitted events in each. An optimum value of b=30 was determined so that the test best discriminates between the distribution 4.3.3-3 resulting from the Maximum Likelihood fit and the set of all other possible distributions. A value of χ^2=20 was then calculated, with a corresponding confidence level between 0.52 and 0.92. This indicates an adequate fit in the usual sense.

4.3.4 Monte Carlo Model for Q2B Production

To derive Q2B production cross sections, it is necessary to correct the figures in table 4.3.3-2 for events lost due to the geometrical acceptance of the apparatus. The size of the neutron detector limits the event sample to those for which $\theta_{bn}^{L} \lesssim 3°$. Neutrons resulting from the decay of a baryon resonance, however, can have laboratory angles considerably greater than 3°, depending on the mass of the baryon and the dynamics of its production and decay. Event detection efficiency is determined from the results of Monte Carlo (MC) modeling. The model can also be used to estimate the likelihood for pion misassociation.

For input to the model, it is desirable to assign the quantum numbers of established baryon resonances to the enhancements observed in regions 1, 2, and 3 of figure 4.3.2-1. The only baryon with which the fitted mass of region 1 is consistent is the $N^*(1520)$ $[I(J^P)=\frac{1}{2}(\frac{3}{2}^-)]$. This baryon has also been unambiguously identified by Ferrer (1978) and Abashian (1976) (see table 4.1-1).

The situation for regions 2 and 3 is less clear, for there

are several broad, overlapping resonances that couple to the $(n\pi\pi)$ final state in the mass range 1600 MeV/c^2<$m_{(n\pi\pi)}$<1960 MeV/c^2. The statistics are not high enough to resolve them. In fact, statistical uncertainty will dominate over systematic differences arising from the choice of one resonance or another. For definiteness, the $N^*(1670)$ $[I(J^P)=\frac{1}{2}(\frac{5}{2}^-)]$ and $\Delta(1890)$ $[I(J^P)=\frac{3}{2}(\frac{5}{2}^+)]$ will be associated with regions 2 and 3. The fitted mass and width of region 3 are consistent with the latter; the fitted mass for region 2 is consistent with the former, but the fitted width is considerably smaller than the nominal value of 155 MeV. [Comparisons are made to resonance parameters quoted by the Particle Data Group. See Bricman (1978).]

Support for an $I=\frac{3}{2}$ assignment to region 3 can be had from the following argument: If one assumes that all three regions reflect $I=\frac{1}{2}$ objects, then the expected ratio of $\Delta^+(1236)$ to $\Delta^-(1236)$ events in the $(n\pi_3^+)$ and $(n\pi_4^-)$ mass subspectra is 0.11±0.01. This result is obtained by scaling the fitted number of events in each region with the appropriate Clebsh-Gordan coefficients. If region 3 reflects an $I=\frac{3}{2}$ object, however, the ratio is 0.27±0.04. The observed ratio, obtained from fits to the two mass subspectra, is 0.29. Unfortunately this conclusion is not unambiguous since it is sensitive to the background parameterization in the fits.

The masses for the resonances in a MC event are selected from Breit-Wigner distributions given by Jackson (1964). The central mass values and widths of the distributions are taken from the fit results in table 4.3.3-1.

The exponential slope parameterizing the u_B' distribution for MC events can be estimated from the data. The ansatz is made that all of the Q2B events in the data are distributed in u_B' according to

$$f(u_B') = Ae^{-b|u_B'|}\xi(u_B'), \qquad 4.3.4\text{-}1$$

where ξ gives the effect of the detector as a function of u_B'. Although there are six different Q2B states contributing to the

data, each of which may be associated with a different exponential slope, they are treated in aggregate to gain statistical significance. Knowing the function ξ, one can fit the data for the parameter b.

To obtain $\xi(u'_B)$, MC events uniformly distributed in u'_B (i.e., with b=0) are generated for each Q2B state present in the data. For a particular state j, the number of detected events, d_j, is related to the number of generated events, g_j, by a detection efficiency, ε_j:

$$d_j(u'_B) = \varepsilon_j(u'_B) g_j . \qquad 4.3.4\text{-}2$$

Let d_j be a fraction w_j of the total number of events detected:

$$d_j(u'_B) = w_j \sum_{j=1}^{6} d_j(u'_B) \equiv w_j D(u'_B) . \qquad 4.3.4\text{-}3$$

Then

$$g_j = \frac{w_j}{\varepsilon_j(u'_B)} D(u'_B) . \qquad 4.3.4\text{-}4$$

The total number of events generated is

$$G = D(u'_B) \sum_{j=1}^{6} \frac{w_j}{\varepsilon_j(u'_B)} , \qquad 4.3.4\text{-}5$$

whence

$$D(u'_B) = G \left(\sum_{j=1}^{6} \frac{w_j}{\varepsilon_j(u'_B)} \right)^{-1} . \qquad 4.3.4\text{-}6$$

Comparing equation 4.3.4-6 to equation 4.3.4-1, one finds

$$\xi(u'_B) = \left(\sum_{j=1}^{6} \frac{w_j}{\varepsilon_j(u'_B)} \right)^{-1} . \qquad 4.3.4\text{-}7$$

The factors w_j are taken from the results of the fit to the m_M vs. m_B scatterplot (see equation 4.3.3-4). The detection efficiencies for six MC runs, corresponding to the six Q2B states, are shown in figure 4.3.4-1. Although the effi-

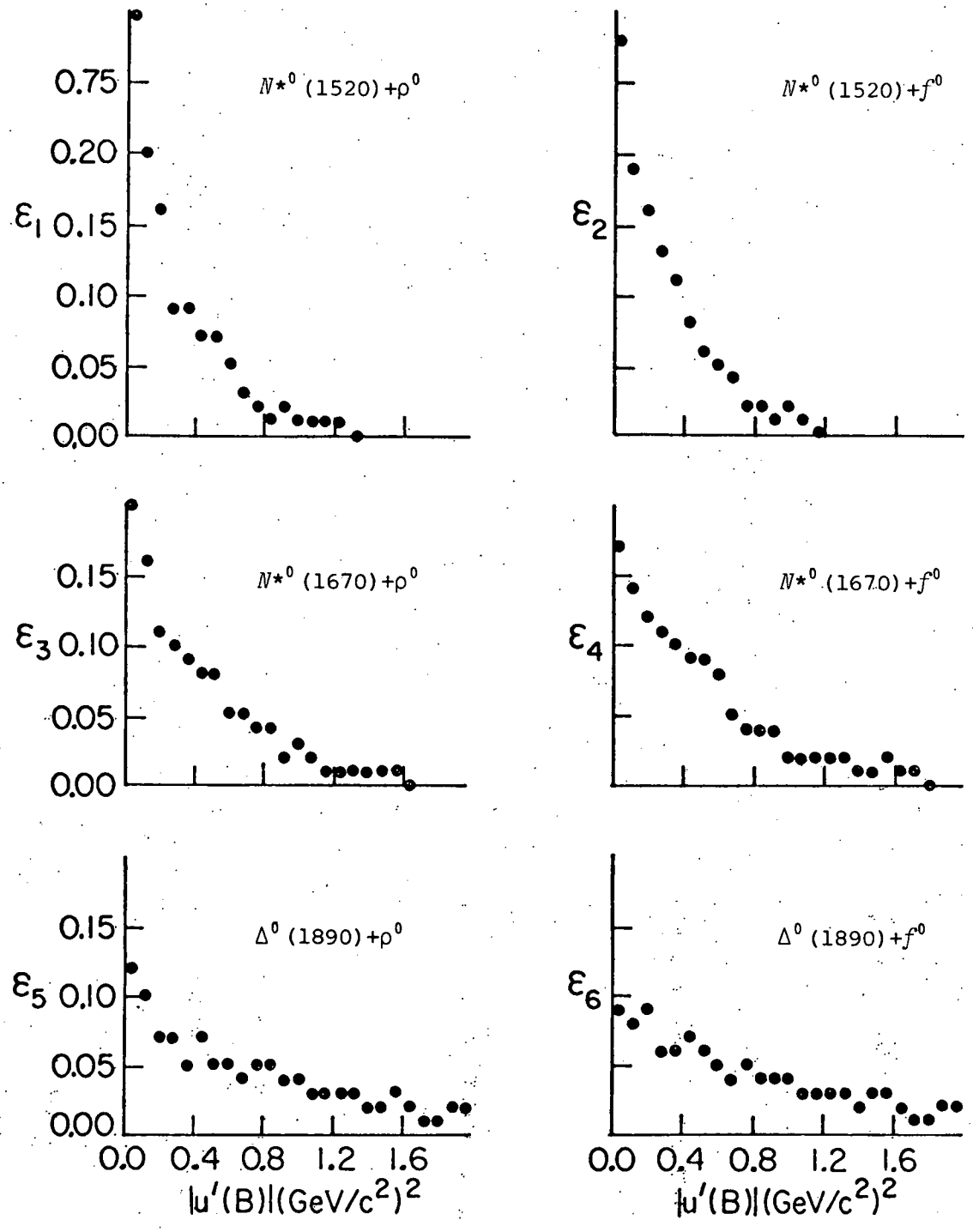

Figure 4.3.4-1 The detection efficiencies for six sets of Monte Carlo events corresponding to the six Q2B states observed in the data. The Monte Carlo events were generated uniformly in u'_B.

ciency is not strongly dependent on the identity of the meson, it decreases considerably in the small $|u'_B|$ region as the mass of the baryon increases.

Equation 4.3.4-1 is expected to more closely approximate the u'_B distribution of the data after a background subtraction has been made to reduce the effect of events not belonging to the six Q2B states modeled. The fit to the $(\pi^+_1\pi^-_2)$ mass distribution admits the possibility that ∿40% of the events are background. Three sources are considered:

(1) Events in which the $(\pi^+_1\pi^-_2)$ pair results from an s-wave interaction, which may account for the enhancement near 1000 MeV/c^2 in figure 4.3.2-2;
(2) Q2B events of the type $(n\pi^+\pi^-)(\pi^+\pi^-)$ in which the pions have been misassociated;
(3) Events not in either of the classes above, specifically those for which the $(\pi^+_1\pi^-_2)$ pair is nonresonant.

There is no tenable procedure for obtaining the u'_B distribution for events in the first category. Events in the latter two categories have a $(\pi^+_1\pi^-_2)$ pair that is nonresonant. It is reasonable to suppose that the $u'_{(n\pi^+_3\pi^-_4)}$ distribution for such events is similar to that for events with a pion pair that is manifestly nonresonant, such as $(\pi^+_1\pi^+_2)$ or $(\pi^-_1\pi^-_2)$. Here the subscripts 1 and 2 indicate pions of like charge that have been labeled by the prescription normally used to discriminate among pion pairs of opposite charge. That is, $(\pi^\pm_1\pi^\pm_2)$ is the pair such that $|u'_{(n\pi^\pm_1\pi^\pm_2)}|$ is the largest of the six possible pion pair combinations.

The u' distribution approximating the background is first smoothed and then weighted so that the total number of events is equal to the number of background events obtained from the fit to the data. Figures 4.3.4-2(a) and (b) show semilogarithmic plots of the $|u'_{(n\pi^+_3\pi^-_4)}|$ distribution before and after the background subtraction. In the latter figure, points beyond $|u'_{(n\pi^+_3\pi^-_4)}| = 0.68$ are within one standard deviation of zero

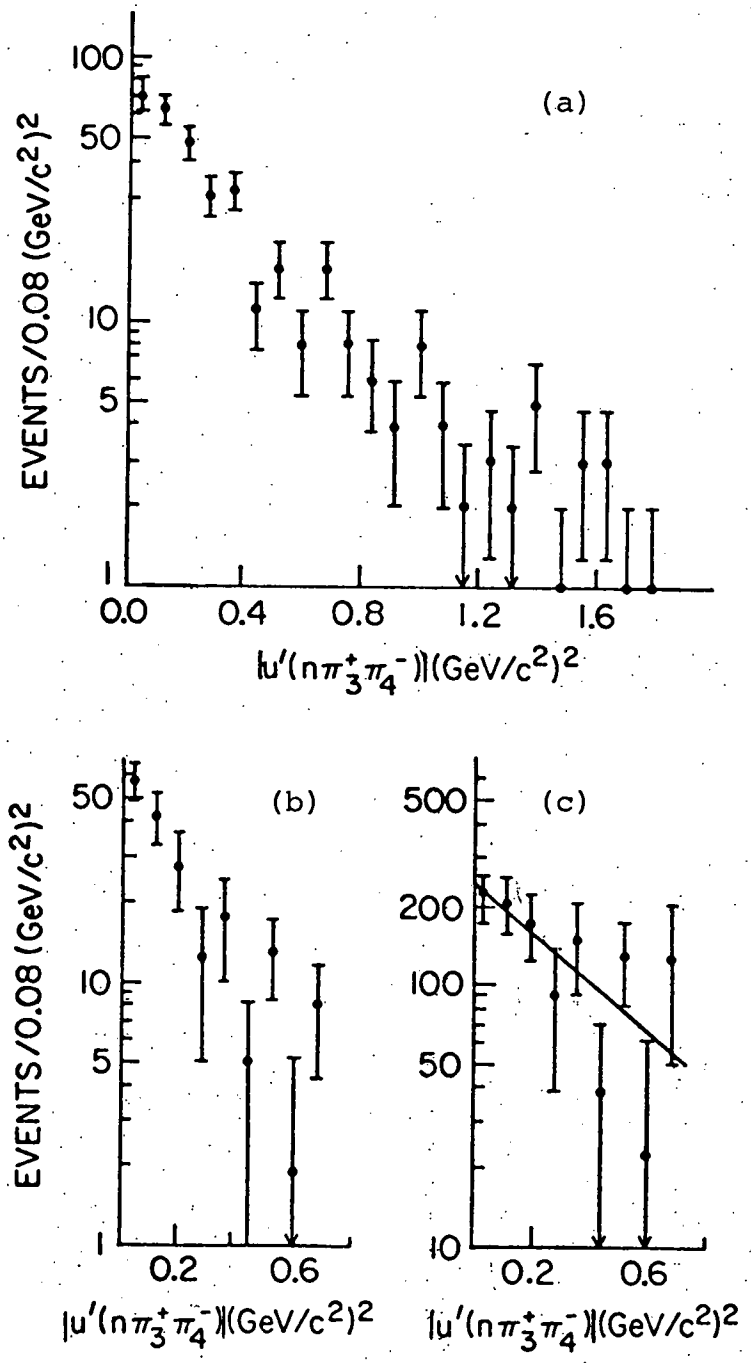

Figure 4.3.4-2 $|u'_{(n\pi_3^+\pi_4^-)}|$ distributions

(a) before subtracting kinematic background
(b) after subtracting kinematic background
(c) after correcting for undetected events. The straight line is a fit to the data with the function $f(u') = A\exp(-b|u'|)$.

and have been suppressed. Figure 4.3.4-2(c) shows the distribution that results when the effect of the detector, given by equation 4.3.4-7, is divided out. The error bars reflect statistical uncertainty, while the straight line is the result of a fit with the function $f(u') = A\exp(-b|u'|)$. One finds that $A = 221.5\pm97.5$ and $b = 2.1\pm1.1$ with a confidence level of 30%.

The angular distribution governing the decay of a MC resonance depends on the spin and parity of the resonance, the spin density matrix of the resonance, and the spins and parities of the decay products. The formalism is discussed by Gottfried (1964). It is assumed that the decay is parity conserving and that the products are in a state of definite orbital angular momentum, ℓ. The value is taken to be the smallest consistent with conservation rules. This is plausible for low mass resonances, where the energy available for the decay relative to the product masses makes it unlikely that higher ℓ-wave states contribute significantly.

The baryon resonance was allowed to decay sequentially via the intermediate state $(\Delta(1236)\pi)$, a process treated by Button - Shafer (1965) and by Berman (1965). The effect of other possible decay modes [e.g., (ρn)] was found not to be important to the predicted overall event detection efficiency.

The spin density matrix, ρ^B, of the baryon resonance is assumed to be diagonal with elements

$$\rho^B_{mm} = \begin{cases} \frac{1}{2}; & |m| = \frac{1}{2} \\ 0; & |m| \neq \frac{1}{2} \end{cases} . \qquad 4.3.4\text{-}8$$

These values are a consequence of the one-particle-exchange picture, described in section 4.1, if the exchanged particle is assumed to be an unpolarized nucleon, and if the axis of quantization is chosen to be the direction of the beam in the baryon rest frame.

Unlike the decay angular distribution of the baryon resonance, that of the meson resonance is not significantly biased

by the geometrical acceptance. For the ρ^0 meson, a moment analysis of 133 observed events having 570 MeV/c^2 < $m_{(\pi_1^+\pi_2^-)}$ < 840 MeV/c^2 gives the following values for the spin density matrix:

$$\begin{aligned} \rho^{\rho}_{0\,0} &= 0.30\pm0.09 \\ \rho^{\rho}_{1\,-1} &= -0.08\pm0.07 \\ \mathrm{Re}\{\rho^{\rho}_{1\,0}\} &= 0.09\pm0.06. \end{aligned} \qquad 4.3.4\text{-}9$$

These numbers reflect the kinematic background subtraction described previously in connection with the determination of the exponential slope, but no attempt has been made to gauge the possible interference of a nonresonant spin-0 background. With only $\rho^{\rho}_{0\,0}$ differing significantly from zero, the results are consistent with the isotropic decay of the ρ^0 meson.

Limited statistics and the relative importance of interference effects preclude a similar analysis for the f^0 meson. The assumption of spin-½ nucleon exchange, however, forces all matrix elements for the f^0 having $|m|=2$ to be zero. Thus, the spin density matrix for both the ρ^0 and f^0 mesons was taken to be

$$\rho^{M}_{mm} = \begin{cases} \frac{1}{3};\ m = 1,0,-1 \\ 0;\ \text{otherwise.} \end{cases} \qquad 4.3.4\text{-}10$$

4.3.5 Results of the Monte Carlo Model

The MC model is based on a subset of the data's features that corresponds directly to the ansatz described in sections 4.1 and 4.3.4. Confidence in the model can be gained by comparing its predictions to features of the data to which it is not specifically tuned. A number of distributions were studied and, in most cases, reasonable agreement between the real data and the MC data was found. For this purpose MC events for the six Q2B states observed in the data were subjected to the

charged pion ordering procedure described in section 4.3.1 and then combined in proportion to the amount of each state in the data. The result was then scaled so that the number of MC events equaled the number of real events. No attempt was made to incorporate a background other than that arising from pion misassociation.

For example, figure 4.3.5-1 shows distributions of the CM opening angle between (a) pions of like charge, (b) positive pions and the neutron, and (c) negative pions and the neutron. The dots are MC points, connected to guide the eye. The inference is that the model adequately describes the geometrical behavior of the final state pions.

Figures 4.3.5-2, 4.3.5-3, and 4.3.5-4 show invariant mass distributions for various final state particle combinations. In each case, the distributions for pions of identical charge have been combined. The most significant systematic deviation of the MC data from the real data appears in figure 4.3.5-4(b). When events with $m_{(n\pi_3^+\pi_4^-)} > 1740$ MeV/c^2 are excluded [those events in region 3 of the $(n\pi_3^+\pi_4^-)$ spectrum], a qualitative improvement results, as shown in figure 4.3.5-4(c). This suggests that regions 1 and 2 contain a relatively pure sample of Q2B events well described by the model. Furthermore, background effects become important in region 3, but not enough to warrant rejection of the model. The cross sections involving the $\Delta^0(1890)$ quoted below should be viewed with this admonition in mind, however.

Table 4.3.5-1 lists the detection efficiency, ordering efficiency, and backward production cross section for the six Q2B states observed in the data. The ordering efficiency is defined as the ratio of the number of MC events having pions correctly paired and $m_{(n\pi_3^+\pi_4^-)} < 1960$ MeV/c^2 to the total number of detected MC events. The cross sections are obtained from a product of the reciprocals of the efficiency factors with the cross section basis (see section 3.4). Those cross sections involving the f^0 have been corrected for unobserved decay modes. A similar correction has not been made for the

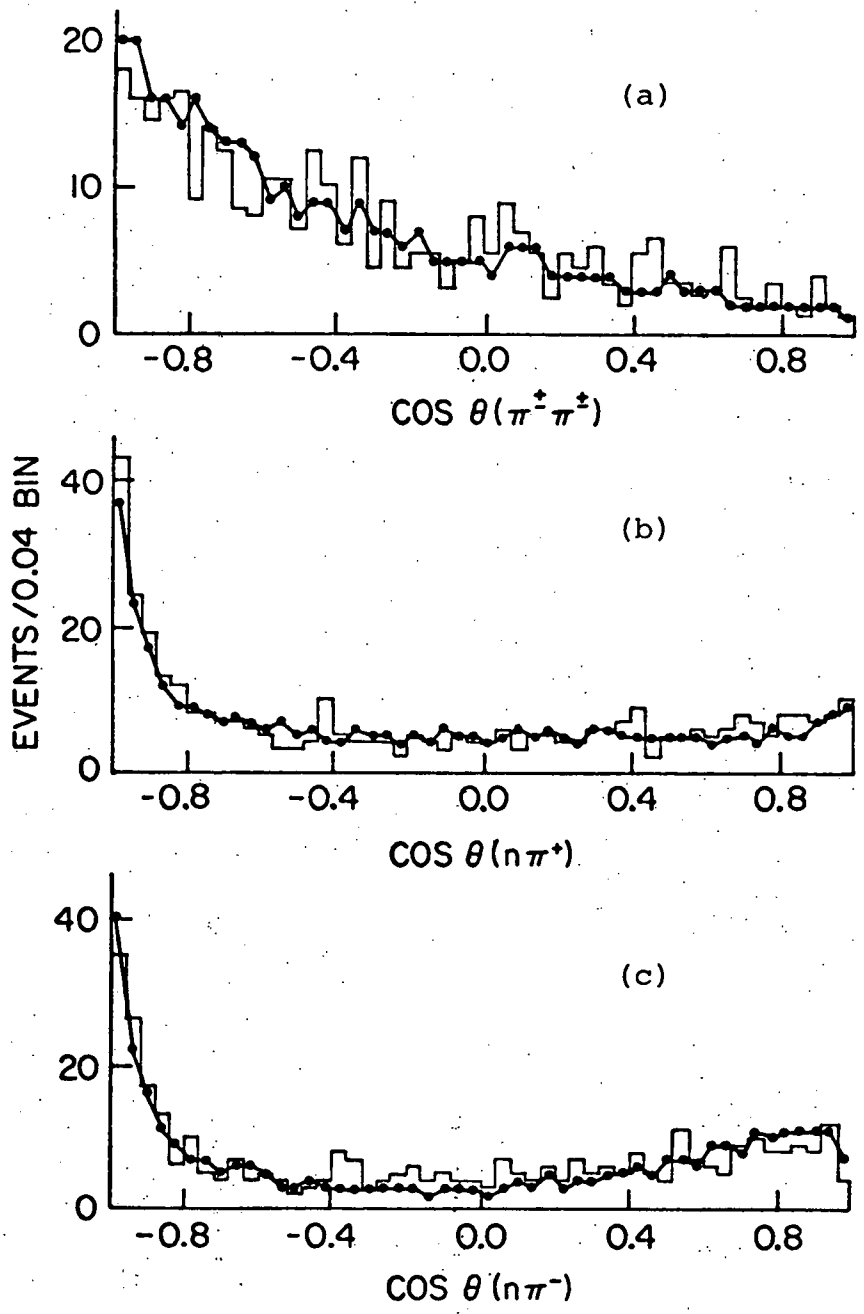

Figure 4.3.5-1 Center-of-momentum opening angle distributions between
(a) pions of like charge, with two entries per event
(b) the neutron and positive pions, with two entries per event
(c) the neutron and negative pions, with two entries per event.
Monte Carlo data (solid points) are superimposed.

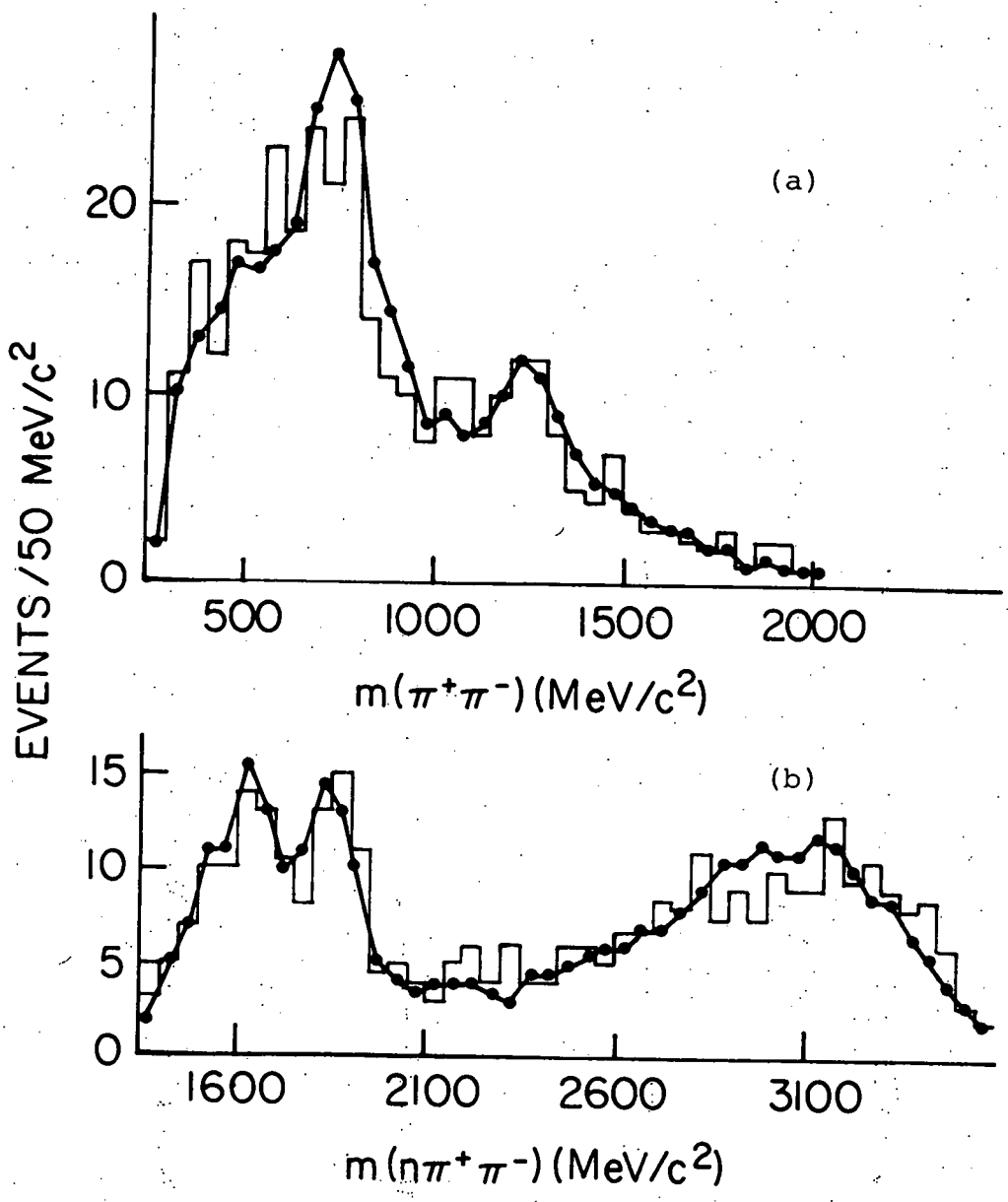

Figure 4.3.5-2 Invariant mass distributions, with four entries per event, of (a) the $(\pi^+\pi^-)$ particle combinations and (b) the recoiling $(n\pi^+\pi^-)$ particle combinations. Monte Carlo data (solid points) are superimposed.

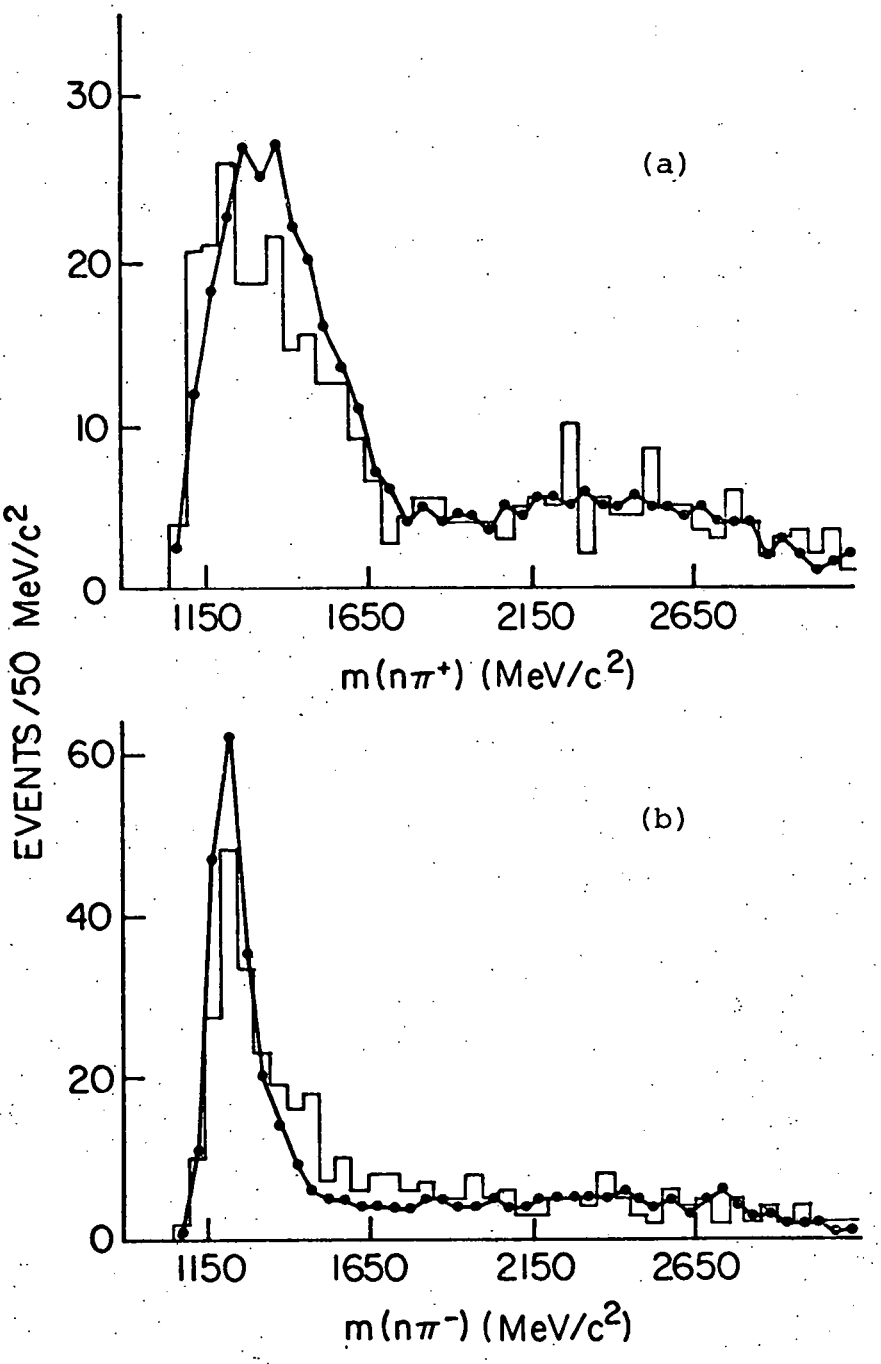

Figure 4.3.5-3 Invariant mass distributions, with two entries per event, of (a) the $(n\pi^+)$ particle combinations and (b) the $(n\pi^-)$ particle combinations. Monte Carlo data (solid points) are superimposed.

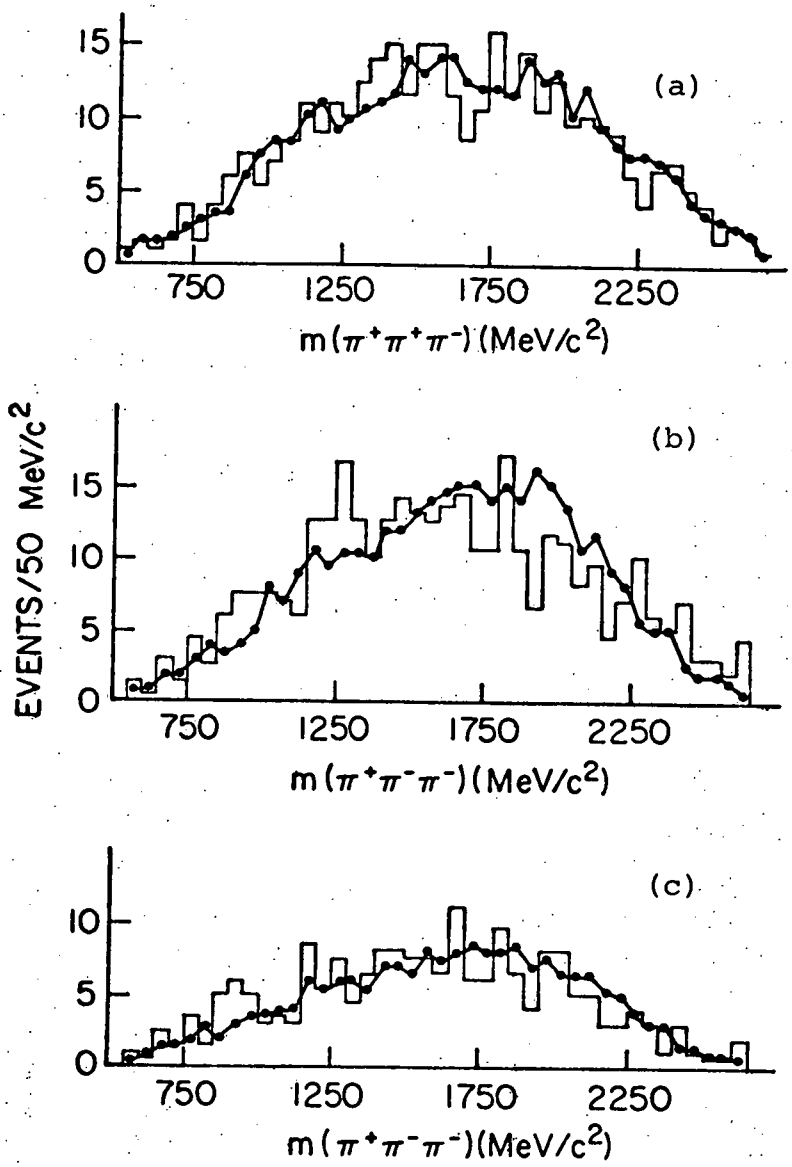

Figure 4.3.5-4 Invariant mass distributions, with two entries per event, of
(a) the $(\pi^+\pi^+\pi^-)$ particle combinations
(b) the $(\pi^+\pi^-\pi^-)$ particle combinations
(c) the $(\pi^+\pi^-\pi^-)$ particle combinations after events having $m_{(n\pi_3^+\pi_4^-)} > 1740$ MeV/c^2 are excluded.
Monte Carlo data (solid points) are superimposed.

baryon, however, due to the uncertainty in its identity. The reader is reminded that the errors on the cross sections do not include a large systematic uncertainty in the cross section basis (~20%, see table 3.4-1), and therefore are dominated by statistics.

Table 4.3.5-1

Q2B State	Detection Efficiency	Ordering Efficiency	σ(μb)
$N^{*0}(1520)+\rho^0$	0.135	0.971	1.49±0.29
$N^{*0}(1670)+\rho^0$	0.105	0.941	0.80±0.18
$\Delta^0(1890)+\rho^0$	0.069	0.793	5.15±0.99
$N^{*0}(1520)+f^0$	0.143	0.784	2.11±0.58
$N^{*0}(1670)+f^0$	0.106	0.663	1.11±0.35
$\Delta^0(1890)+f^0$	0.067	0.549	6.14±1.95

4.4 The $(n\pi^-)(\pi^+\pi^+\pi^-)$ Channel

4.4.1 Pion Discrimination

Based on figure 4.2-2(a), one expects Q2B production in this channel to be characterized by a $\Delta^-(1236)$ baryon accompanied by a 3-pion meson resonance. Let π_4^- (π_3^-) be the negative pion associated with the baryon (meson) resonance, with π_4^- chosen so that $m_{(n\pi_4^-)}$ is in the Δ-region: $m_{(n\pi_4^-)} < 1360$ MeV/c^2. There are 43 events for which both $(n\pi^-)$ combinations are in the Δ-region. In this case, let $(n\pi_4^-)$ be the more backward of the two combinations: $|u'_{(n\pi_4^-)}| < |u'_{(n\pi_3^-)}|$

4.4.2 Evidence for Q2B Production

The procedure above selects 413 events out of the 749 event sample. Figure 4.4.2-1(a) shows their $(\pi_1^+\pi_2^+\pi_3^-)$ mass distribution. An enhancement possibly indicative of the A_2^+ meson is visible at 1300 MeV/c^2. The enhancement at 1550 MeV/c^2 cannot be attributed to a known 3-pion resonance. It is likely, however, that these events are a reflection of low mass N^{*0}/Δ^0

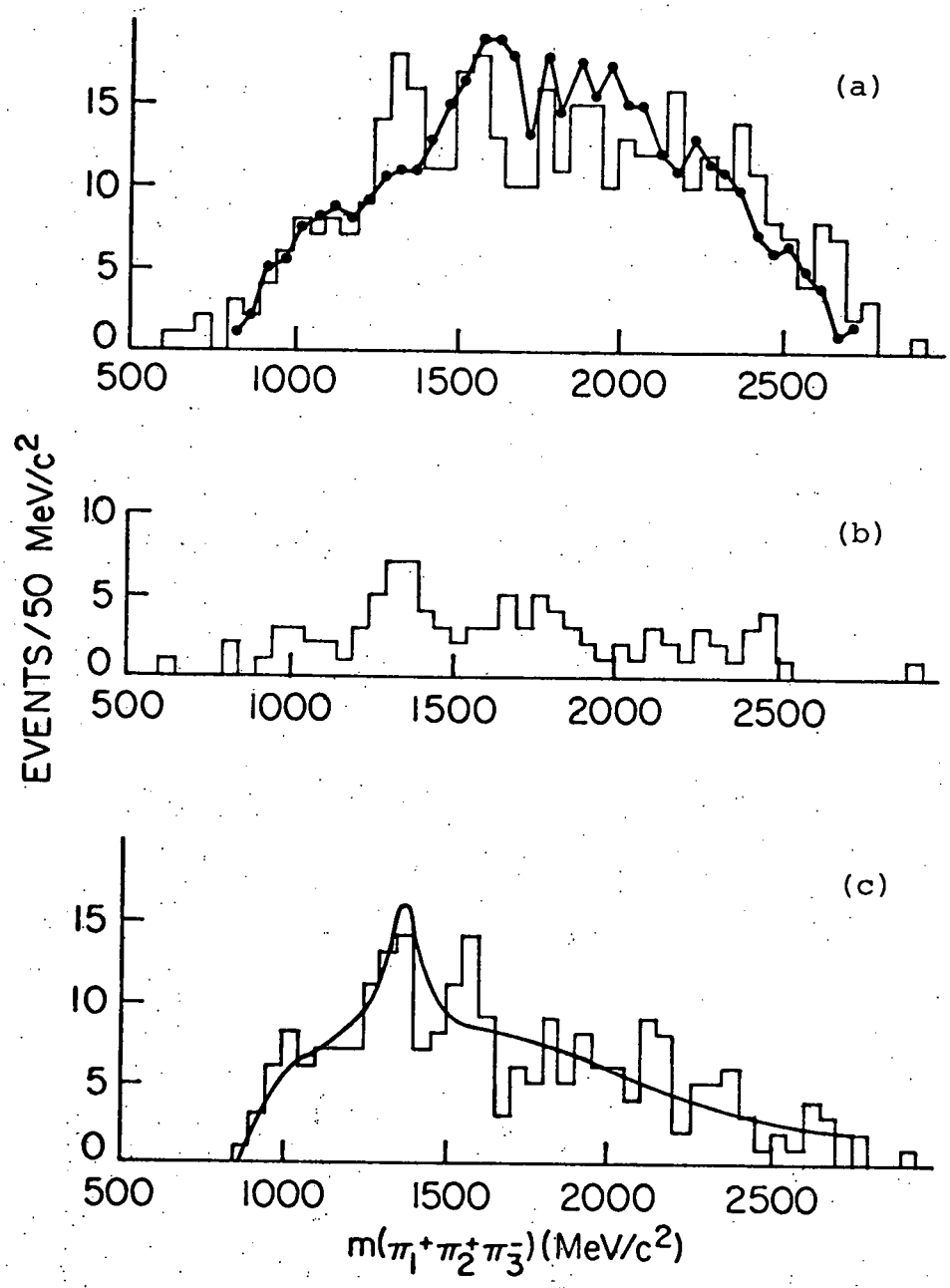

Figure 4.4.2-1 Invariant mass distributions of the $(\pi_1^+\pi_2^+\pi_3^-)$ particle combination

(a) with data from Monte Carlo events of the type $N^{*0}/\Delta^0+\rho^0/f^0$ superimposed

(b) after events having $m_{(n\pi_4^-\pi^+)}$ <1960 MeV/c^2 are excluded

(c) after events having $m_{(\pi^+\pi_3^-)}$ in the ρ-region are selected. The solid curve is a fit to the data with a single Breit-Wigner function plus a polynomial background function.

$(n\pi^+\pi^-)$ resonances. These baryons which couple strongly to the $(\Delta\pi)$ decay mode will significantly contaminate the Δ-region in the $(n\pi^-)(\pi^+\pi^+\pi^-)$ channel. This contention is borne out by the Monte Carlo model described in section 4.3.4. When MC events of the type $N^{*0}/\Delta^0+\rho^0/f^0$ are subjected to the ordering scheme above, there results the $(\pi_1^+\pi_2^+\pi_3^-)$ distribution demarked by the points in figure 4.4.2-1(a). It mirrors the real distribution well except around 1300 MeV/c^2. If one attempts to reduce this important background by eliminating events having a low $(n\pi_4^-\pi^+)$ mass (< 1960 MeV/c^2), only 98 events remain from which statistically significant information cannot be extracted. This distribution is shown in figure 4.4.2-1(b). Note that an enhancement at 1300 MeV/c^2 remains. There is no evidence for a narrow A_1^+ meson in figure 4.4.2-1(a), although a broader effect could contribute to events in the shoulder just above 1000 MeV/c^2.

Since the A_2^+ decays mainly via the intermediate state $(\rho\pi)$, an enriched sample of these mesons can be obtained by considering those events for which either $(\pi^+\pi_3^-)$ combination falls in the ρ-region: 600 MeV/c^2 < $m_{(\pi^+\pi_3^-)}$ < 900 MeV/c^2. Such events are shown in figure 4.4.2-1(c). The cut results in a substantial reduction in the high mass background, while the features discussed above are essentially unchanged. Again, reflections from $N^{*0}/\Delta^0+\rho^0$ Q2B events are important.

4.4.3 Fits to the Data

The nature of the background precludes extraction of definitive information regarding the A_1^+ meson. Therefore, the data of figure 4.4.2-1(c) were fit with a single nonrelativistic Breit-Wigner function for the A_2^+ meson, plus a background function of the form

$$f_{BG}(m) = (m-m_0)^{\alpha}(m_1-m)^{\beta}\sum_{i=0}^{2}\gamma_i m^i, \qquad 4.4.3\text{-}1$$

where m_0 and m_1 were fixed at the lower and upper limits of the distribution. The central mass value of the Breit-Wigner function was allowed to vary, but the width was fixed at 102 MeV, the value quoted by Ferrer (1978). The fit, shown by the curve

in figure 4.4.2-1(c), yields a mass of 1343±24 MeV/c^2 for the A_2^+ with a confidence level of 47%. There are 23.7±10.5 events associated with the resonance, obtained from an integration over the mass range of the distribution. The errors are statistical. Ignoring the contribution to the fit from the enhancement at 1550 MeV/c^2 does not result in an improvement or in a significant change in the fit parameters.

4.4.4 Cross Section Determination

Reliance is again made on a Monte Carlo model for $\Delta^-(1236)+A_2^+$ Q2B production to correct the number of observed events for acceptance losses. The general outline of the model has been given in section 4.3.4

The virtual baryon mediating the interaction is assumed to be an unpolarized nucleon ($I=\frac{1}{2}$). Although conservation rules do not preclude the exchange of a baryon with $I=\frac{3}{2}$, the data do not support the dominance of this isospin exchange amplitude. If this were the case, and if one naively assumes that the cross sections for the production of the charge conjugate Q2B states ($\Delta^- A_2^+$) and ($\Delta^+ A_2^-$) are related by isospin coupling coefficients, one would expect the observed ratio of A_2^- events to A_2^+ events to be unity. Figure 4.4.4-1 shows the ($\pi^+\pi^-\pi^-$) mass distribution corresponding to the ($\pi^+\pi^+\pi^-$) mass distribution in figure 4.4.2-1(c). There is no evidence of an A_2^- enhancement in the former at the level of the A_2^+ enhancement in the latter. On the other hand, one can not rule out a substantial contribution from $I=\frac{3}{2}$ exchange. If the $I=\frac{3}{2}$ and $I=\frac{1}{2}$ exchange amplitudes were equal, the ratio above would drop to 0.15, which is not inconsistent with the data. This ambiguity is reflected in the error on the detection efficiency quoted below.

The slope parameterizing the u_B' distribution 4.1-2 is taken from Ferrer (1978) to be -2.1 (GeV/c^2)$^{-2}$. The A_2^+ resonance is assumed to decay via the intermediate state ($\rho^0\pi^+$) with orbital angular momentum $\ell=2$.

So constructed, the model predicts a detection efficiency

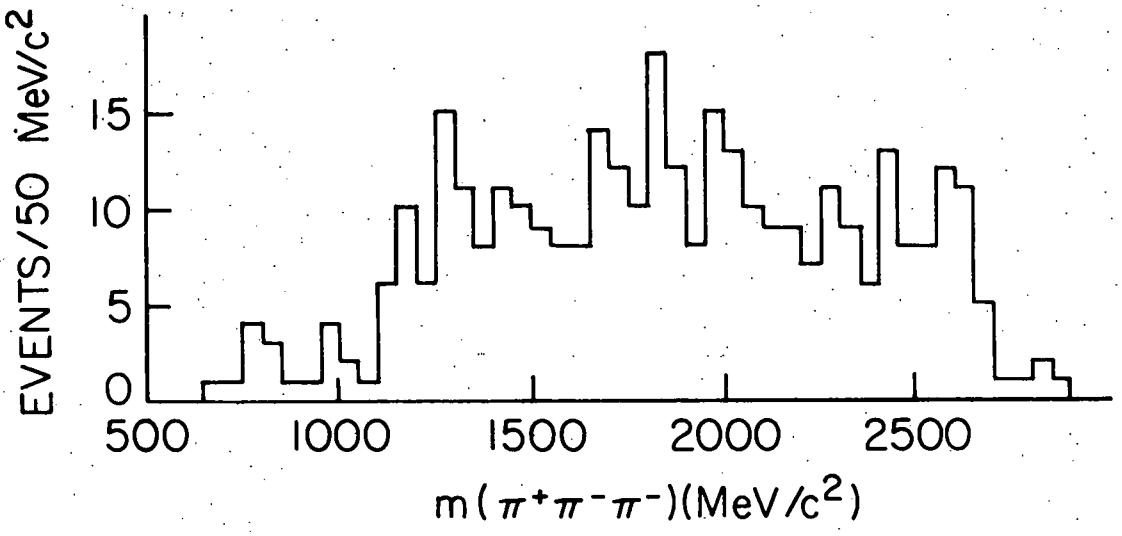

Figure 4.4.4-1 The invariant mass distribution charge conjugate to the $(\pi_1^+\pi_2^+\pi_3^-)$ mass distribution.

of 0.14±0.02 and an ordering efficiency of 0.79. The latter quantity is defined as the ratio of the number of MC events for which the procedure of section 4.4.1 correctly discriminates between the two negative pions and for which 600 MeV/c^2<$m_{(\pi^+\pi_3^-)}$< 900 MeV/c^2 to the total number of detected MC events. The corresponding cross section for ($\Delta^- A_2^+$) Q2B production, corrected for unobserved decay modes of the meson, is 2.51±1.22 μb. Note that here again the systematic uncertainty in the cross section basis discussed in section 3.4 has been omitted from the calculation of the error on the cross section.

4.5 Comparison to Another Experiment

Ferrer (1978) quotes total backward production cross sections for the two Q2B intermediate states $N^{*0}(1520)+\rho^0$ and $N^{*0}(1520)+f^0$ at both 9 and 12 GeV/c , which may be compared to those for the same two intermediate states in this experiment. In both cases, the identification of the $N^{*0}(1520)$ baryon is relatively unambiguous. Table 4.5-1 lists the cross sections, σ_0 , a factor to correct for unobserved decay modes of the baryon, the corrected cross sections, σ_1 , and the laboratory beam momentum, p_b^L :

Table 4.5-1

Q2B State	σ_0 (μb)	Correction Factor	σ_1 (μb)	p_b^L (GeV/c)
$N^{*0}(1520)+\rho^0$	1.49±0.29	4.74	7.06±1.37	8
	0.78±0.18	2.73	2.13±0.49	9
	0.26±0.09	2.73	0.71±0.25	12
$N^{*0}(1520)+f^0$	2.11±0.58	4.74	10.00±2.75	8
	1.18±0.30	2.73	3.22±0.82	9
	0.37±0.11	2.73	1.01±0.30	12

It should be emphasized that in both cases the cross sections do not include a sizable uncertainty in the normalization (∿12% for

Ferrer and ∿20% for this experiment). The final states (see table 4.1-1) and geometrical acceptance also differ.

Nevertheless, it is interesting to note that the energy dependence of the cross section is well described by a simple power law: $\sigma_1 \sim s^{-n}$, where s is the CM energy squared. A fit to the three points for each state gives $n_\rho = 5.7 \pm 1.5$ with a confidence level of 35%, and $n_f = 5.7 \pm 1.3$ with a confidence level of 60%. This observation has little theoretical import because the u_B dependence of the cross section has been integrated out. When Q2B data of other backward reactions at multiple energies are compared [by B. Eisenstein (private communication)], however, similar behavior with commensurate values of n is found.

APPENDIX

A1. Monte Carlo Event Detection

Whether an event produced according to the model described in section 4.3.4 is detected depends on the trajectories of the five final state particles with respect to elements of the experimental apparatus. Each particle in an MC event is subjected to four tests that reflect the different aspects of this geometrical relationship. There are thus twenty tests for each MC event, which have the form

$$\varepsilon_i(\vec{p}_j^{\,L}) \leq r_k, \qquad \text{A1-1}$$

where j indexes the final state particles and the r_k are a set of 20 random numbers between 0 and 1. ε_i, which can be derived from the set of well-measured (real) events, gives the probability that a particle passes the ith test. If any one of the conditions A1-1 is true, the MC event is lost.

A1.1 Flaring

An event is lost when a charged particle, produced at a small angle relative to the streamer chamber's electric field, causes an electrical discharge, or flare, that overexposes the film. The probability for flaring is a function of the angle, θ_E, between a track and the electric field. It was obtained with the method described by Abashian (1976) and is given by

$$P_F(\theta_E) = \begin{cases} 1 & ; \ 0° \leq \theta_E < 15° \\ (40-\theta_E)/25 & ; \ 15° \leq \theta_E < 40° \\ 0 & ; \ 40° \leq \theta_E < 90°. \end{cases} \qquad \text{A1.1-1}$$

The same function applies for $\theta_E' = 180°-\theta_E$.

For charged tracks, then,

$$\varepsilon_1(\vec{p}_j^{\,L}) = 1-P_F; \quad j = 1,\ldots,4 \qquad \text{A1.1-2(a)}$$

and for the neutron

$$\varepsilon_1(\vec{p}_5^{\,L}) = 1. \qquad \text{A1.1-2(b)}$$

A1.2 Shadowing

An event is lost when a charged particle is produced at such an angle that its track is partially or totally obscured (shadowed) by the opaque target box. A MC event particle is propagated through the magnetic field of the streamer chamber from its production point until it exits the chamber. Knowing the particle's trajectory and the configuration of the target box relative to the cameras, one can compute the particle's visible track length, ℓ_v, in each of the three views. In the data it is observed that the minimum visible track length is $\sim$12 cm. Thus

$$\varepsilon_2(\vec{p}_j^{\,L}) = \begin{cases} 0; \ \ell_v < 12 \text{ cm in more than one view} \\ 1; \ \ell_v > 12 \text{ cm in at least two views} \end{cases} \qquad \text{A1.2-1(a)}$$

for charged tracks, and, for the neutron,

$$\varepsilon_2(\vec{p}_5^{\,L}) = 1. \qquad \text{A1.2-1(b)}$$

A1.3 Veto Counters

A charged particle may exit the streamer chamber with a trajectory causing it to strike one of the counters in anti-coincidence with the trigger (see section 2.1.5). If a straight line extrapolation of a MC event particle from its exit point intersects the planar area of a veto counter, then $\varepsilon_3(\vec{p}_j^{\,L})=0$. Otherwise $\varepsilon_3(\vec{p}_j^{\,L})=1$. For the neutron, $\varepsilon_3(\vec{p}_5^{\,L})=1$.

A1.4 Spark Chamber Geometry

The factors described above account for approximately 5% of the MC event losses. The predominant factor is the failure of the neutrons to strike the spark chamber system. Not every

neutron incident on the system, however, is detected. The efficiency for the system to convert neutrons to charged secondaries with sufficient penetrating power to reach the scintillation counters was determined by an independent Monte Carlo analysis described in section A2 of this Appendix. In addition to this, there is the purely geometrical effect that a neutron incident near the edge of the system is less likely to result in a trigger than a neutron incident near the center.

Figure A1.4-1 maps η, the geometrical efficiency, in the plane defined by the first plate of the first (most upstream) spark chamber. The chamber's center is at $y'=z'=0$. The map is symmetric about the y' and z' axes, so only the first quadrant is shown. The map was derived from a sample of neutron interactions within the chambers culled from the data. The sample was restricted to neutrons with $p_n^L \simeq 8$ GeV/c incident near the center of the system in order to minimize inherent geometrical bias and momentum dependent effects. Each interaction was parameterized by the interaction position, the trajectories of the charged secondaries, and their ranges.

To each point (y',z') in the plane of the first spark chamber plate at $x=x'$, there corresponds a point $(y_i(x_i,x',z'),z_i(x_i,x',z'))$ in the plane of the ith interaction at $x=x_i$, as sketched in figure A1.4-2. The trajectories of the charged particles are rotated about a unit vector in the x direction in a series of discrete steps. At each step the secondaries are extrapolated a distance commensurate with their observed ranges to see if a trigger would occur, the requirement being that two out of the three scintillation counters are hit. The likelihood of a trigger for the ith interaction at (y_i,z_i) is given by the ratio of the number of steps for which the requirement is satisfied, $n(y_i,z_i)$, to the total number of steps, N_s. The geometrical efficiency at (y',z') is now computed from

$$\eta(y',z') = \frac{1}{N}\sum_{i=1}^{N}\frac{n(y_i,z_i)}{N_s}, \qquad \text{A1.4-1}$$

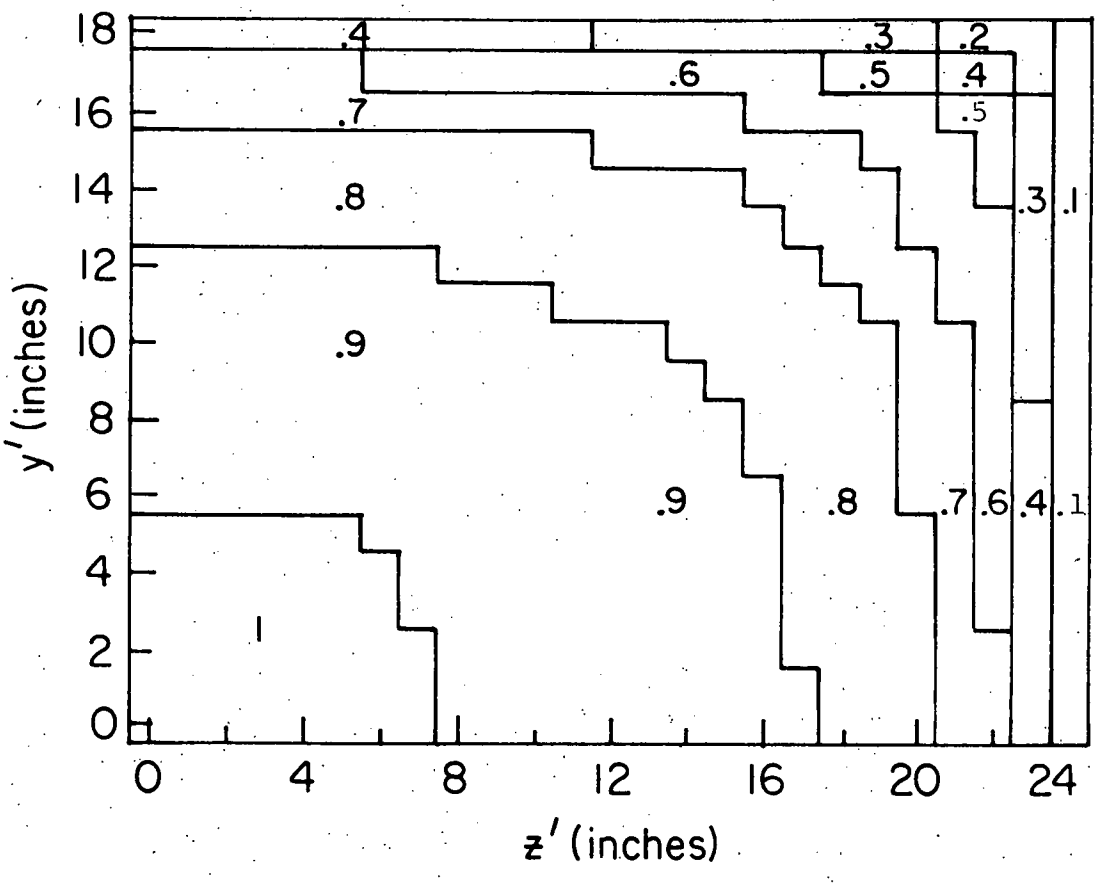

Figure A1.4-1 A map of the efficiency of the spark chamber system to detect charged secondaries from a neutron interaction as a function of the point, (y',z'), at which the neutron intersects the first plate of the first spark chamber. The center of the plate is at (0,0).

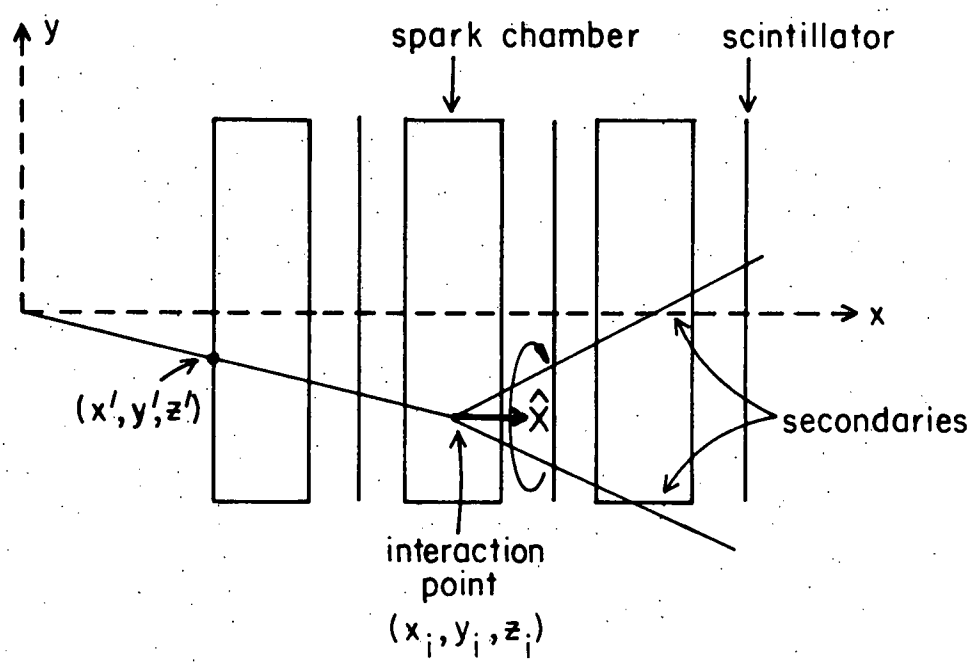

Figure A1.4-2 The geometry of a neutron interaction in the spark chamber system upon which the efficiency calculation is based.

where N is the number of interactions considered.

The MC model described in section A2 predicts one linear momentum dependence of the geometrical efficiency for p_n^L between 2 and 6 GeV/c and another between 6 and 8 GeV/c. This may be incorporated into the factor ε_4 with the result

$$\varepsilon_4(\vec{p}_j^{\,L}) = \begin{cases} 1 & ; j = 1,\ldots,4 \\ 0 & ; j = 5, \text{ neutron misses chambers} \\ (\frac{1}{2}p_5^L - 3)\eta_8 + (4 - \frac{1}{2}p_5^L)\eta_6 & ; 6 \text{ GeV}/c < p_5^L < 8 \text{ GeV}/c \\ (\frac{1}{4}p_5^L - \frac{1}{2})\eta_6 + (\frac{3}{2} - \frac{1}{4}p_5^L)\eta_2 & ; 2 \text{ GeV}/c < p_5^L < 6 \text{ GeV}/c, \end{cases} \qquad \text{A1.4-2}$$

where η_8 (η_6,η_2) is the geometrical efficiency at 8 (6,2) GeV/c. η_6 and η_2 are calculated as in equation A1.4-1, but with MC data.

A2. Spark Chamber Efficiency from a Hadron Cascade Model

The factor W_6 that enters into the calculation of the cross section normalization (see section 3.4) gives the probability that an 8 GeV/c neutron normally incident on the center of the spark chamber system will interact and produce charged secondaries sufficiently penetrating to cause a trigger. It was determined from a model for the development of a hadron cascade within the system, based on an adaptation of the work of Baroncelli (1974), Jones (1969), and Ranft (1972).

A2.1 Description of the Model

Only nucleons and pions were considered. In particular, the decay of a π^0 into two photons and subsequent e^+e^- pair production was ignored, primarily because there was little empirical evidence that such a process caused many triggers. The probability distributions governing the behavior of the hadrons are not necessarily well-founded theoretically, but reflect a consolidation of disparate experimental data, which is discussed in the references above. The constants appearing in the distributions are listed in table A2.1-1. Confidence in the model was gained from its stability with respect to variations in these constants, and from checks against features of the spark chamber data.

The composition of each spark chamber was approximated by a homogeneous medium with density a quarter that of iron. This represents a weighted average of the steel plate-gas gap array. The effect of the aluminum plates at the front and rear of each chamber was insignificant. Hadrons were assumed to interact only within the chambers. Interactions within the scintillation counters separating the chambers, in their light pipes, and in the chamber support structure were considered and found to be unimportant.

The distance, d, from a hadron's point of origin within a chamber to its point of interaction was selected from the distribution

$$P(d) = \frac{1}{\lambda} e^{-d/\lambda}, \qquad \text{A2.1-1}$$

where λ is the nuclear absorption length appropriate for the chamber medium. Between production and interaction, a hadron was assumed to move in a straight line and, if charged, to lose energy to ionization at a rate dependent on its mass and the medium's density. If at the point of interaction a hadron's energy, E_I, was less than a certain threshold value, E_{min}, an interaction did not occur and the hadron's propagation terminated (ranged out). If d exceeded the distance to the nearest boundary of the chamber, the hadron exited the chamber without interacting, whereupon it could strike a scintillation counter and then enter another chamber. Whenever a charged hadron struck a scintillator, a hit was recorded. Two hits defining a trigger caused generation of the cascade to be terminated. The cascade could cease without a trigger if all hadrons ranged out or left the system without interacting. The ratio of the number of triggers to the number of incident neutrons gives the efficiency.

Upon interacting, a hadron surrendered an amount of energy

$$E_{nf} = \begin{cases} 124N_{nf} + 30 & ; \; E_I > 1000 \text{ MeV} \\ 37N_{nf} + 4N_{nf}^2 & ; \; E_I < 1000 \text{ MeV} \end{cases} \qquad \text{A2.1-2}$$

to nuclear fragmentation. N_{nf} is the number of nuclear fragments, selected from a Poisson distribution with mean

$$\langle N_{nf} \rangle = 2.1 A_{Fe}^{0.19} E_I^{1/3}, \qquad \text{A2.1-3}$$

where A_{Fe} is the atomic mass number of iron.

The number of secondary pions, N_π, resulting from an interaction was selected from a Poisson distribution with mean

$$\langle N_\pi \rangle = \kappa A_{Fe}^{0.19} E_I^{1/2}. \qquad \text{A2.1-4}$$

In addition to pions, one secondary nucleon resulted from an interaction, but only if the interacting hadron was itself a nucleon.

A secondary nucleon was assumed equally likely to be a proton or neutron. The identity of a secondary pion was selected from the binomial distribution so that, on average, and subject to charge conservation, $\frac{2}{3}$ were charged and $\frac{1}{3}$ were neutral. No distinction was made between a π^+ and a π^-.

The secondary nucleon was produced with energy

$$E_N = \alpha E_I - E_{nf}, \qquad \text{A2.1-5}$$

where α was selected from the beta distribution

$$P(\alpha) = \frac{\Gamma(a+b+2)}{\Gamma(a+1)\Gamma(b+1)} \alpha^a (1-\alpha)^b. \qquad \text{A2.1-6}$$

The constants a and b depend on the properties of the medium. The energy, E_π^i, of the ith secondary pion was selected from the distribution

$$P(E_\pi^i) = \frac{1}{T} \exp(E_\pi^i/T), \qquad \text{A2.1-7}$$

where $T = (1-\alpha)E_I/N_\pi$. The energies were subjected to the constraint that

$$\sum_{i=1}^{N_\pi} E_\pi^i = (1-\alpha)E_I. \qquad \text{A2.1-8}$$

The magnitude of a secondary's transverse momentum (with respect to that of the interacting hadron) was selected from

$$P(p_t) = p_t \exp(-Bp_t). \qquad \text{A2.1-9}$$

The longitudinal momentum was then fixed by energy conservation. No attempt was made to conserve momentum rigorously. Instead $\hat{p}_t$ was selected from a uniform distribution between 0 and 2π, so that on average the sum of the secondaries' trans-

verse momenta was zero.

Table A2.1-1

Constant	Nucleon	Pion	Reference
ρ_{Fe} (g/cm^3)	7.87	7.87	---
λ (cm)	70.65	83.86	Baroncelli (1974)
E_{min} (GeV)	1.0	0.5	Baroncelli (1974)
A_{Fe}	55.85	55.85	---
κ	0.70	0.73	Jones (1969)
a	4.4	---	Jones (1969)
b	2.6	---	Jones (1969)
B (GeV/c)$^{-1}$	5.04	6.037	Baroncelli (1974) Ranft (1972)

A2.2 Results of the Model

The hadron cascade model described above predicts a neutron conversion and detection efficiency for the spark chamber system of $\eta_0 = 0.37 \pm 0.05$. The error is an estimate of the systematic uncertainty and was obtained as follows:

From independent variations in the constants listed in table A2.1-1 as well as in those specifying the size and orientation of the spark chamber system, it was found that the efficiency was most sensitive to the value of λ, the absorption length. This constant, however, reflects the assumption that a spark chamber can be approximated by a continuous, homogeneous medium. In an attempt to justify this approximation, a sample of spark chamber film showing protons incident on the system was examined. This sample was a subset of the 8000 events gathered with an LH_2 target interaction trigger for which the neutron signal requirement was suppressed. Let N_0 be the number of protons incident on a chamber and N be the number observed to penetrate the chamber without interacting. Then an estimate of the absorption length is provided by

$$\lambda = - \frac{\ell}{\ln(N/N_0)} \ , \qquad \text{A2.2-1}$$

where ℓ is the depth of the chamber. One finds λ = 84.0 cm, which differs from the value used in the model by 19%. Taking this to be the uncertainty in λ, one obtains the uncertainty in the efficiency quoted above.

The model can also be used to predict the geometrical efficiency of the spark chamber system. The result should be consistent with that obtained from the data, as described in section A1.4. Figure A2.2-1 plots the geometrical efficiency, η, as a function of y', the distance from the system's center along the y axis. z' is fixed at zero (see figure A1.4-2). The solid points correspond to the data. The error bar gives an indication of the RMS deviations from the values calculated according to equation A1.4-1. The circles correspond to spark chamber events from the hadron cascade model in which 8 GeV/c neutrons were assumed to be normally incident on the center of the system. These MC events were then treated in the same manner as real events.

Alternatively, MC events may be generated in which neutrons are incident at each point in the plane of the first spark chamber plate, rather than at the center only. Let $\eta'(y',z')$ be the ratio of the number of MC neutrons that result in a trigger to the number of MC neutrons incident at the point (y',z'). By definition, $\eta'(0,0)=\eta_0$. Thus, the quantity $\eta'(y',z')/\eta_0$ gives another measure of the geometrical efficiency, factors independent of geometry having been divided out. Figure A2.2-2 compares η'/η_0 (circles) to η (solid points), where, once again, η is the efficiency obtained from the real data according to equation A1.4-1 and the comparison is made at $z'=0$. The error bar gauges the uncertainty in the MC points due to the error in η_0. In both figures A2.2-1 and A2.2-2 reasonable agreement between the real data and the MC data can be seen.

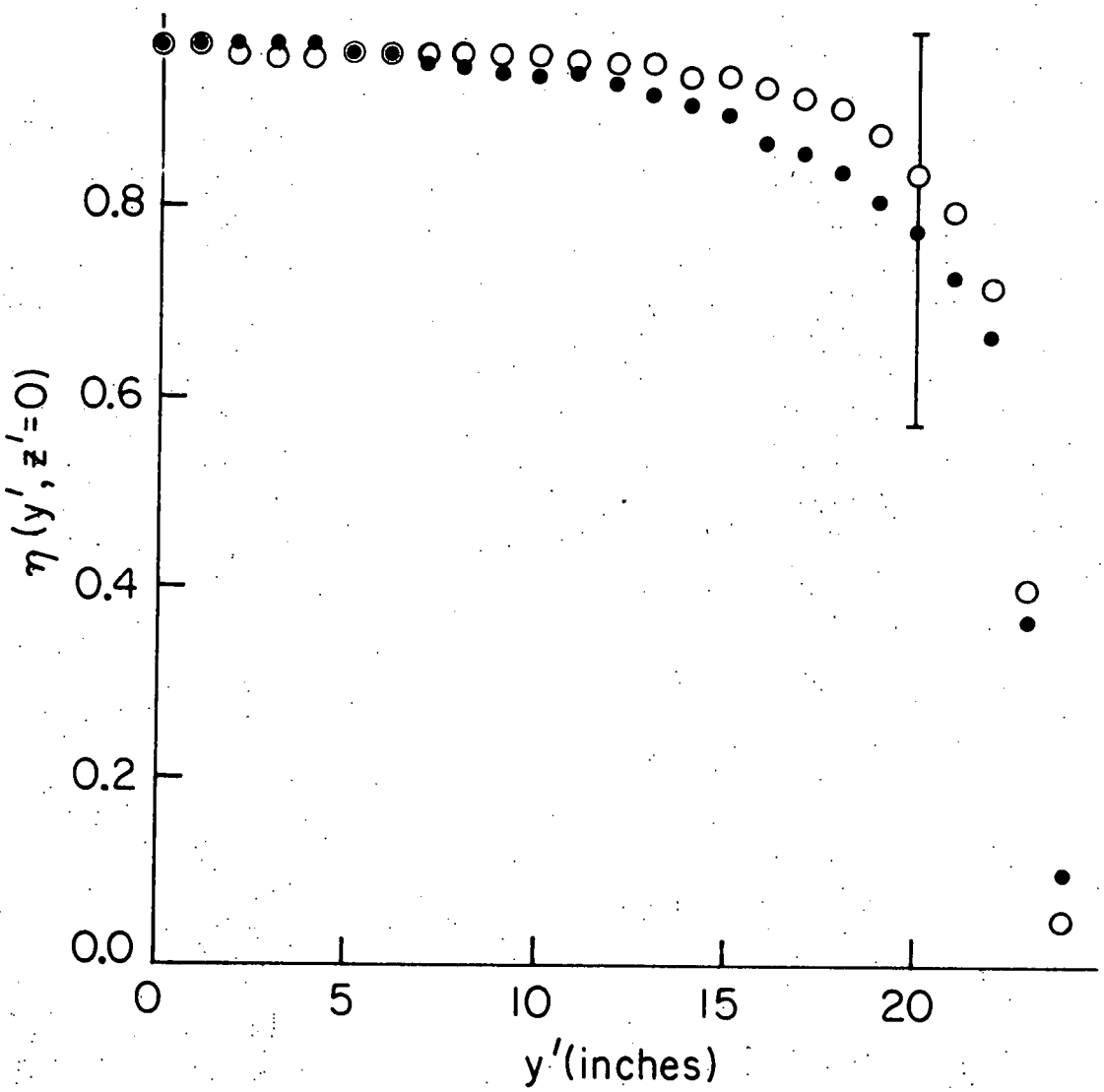

Figure A2.2-1 The efficiency of the spark chamber system to detect charged secondaries from a neutron interaction as a function of the distance from the center of the system, derived from real data (solid points) and from Monte Carlo data (circles).

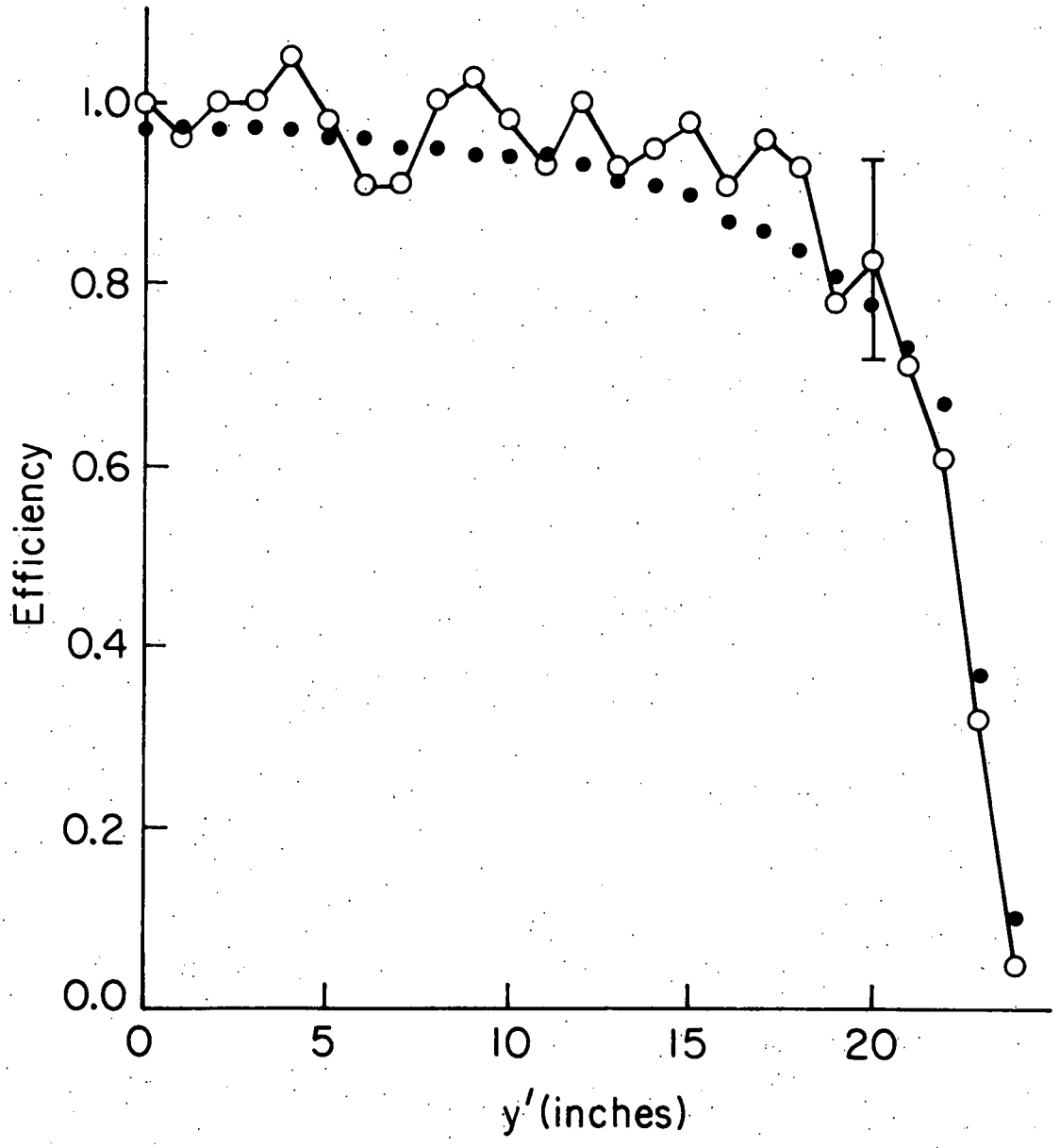

Figure A2.2-2 A comparison of η (solid points) to η'/η_0 (circles), where both quantities gauge the efficiency of the spark chamber system to detect charged secondaries from a neutron interaction as a function of the distance from the center of the system.

REFERENCES

Abashian, A., *et al.*, 1976, Phys. Rev. D13, 5.

Abashian, A., *et al.*, 1974, Nucl. Instrum. Methods 115, 445.

Amaglobeli, N.S., *et al.*, 1977, Sov. J. Nucl. Phys. 25, 523.

Arenton, M.W., *et al.*, 1978, Nucl. Phys. B141, 77.

Barger, V.D. and D.B. Cline, 1969, *Phenomenological Theories of High Energy Scattering* (Benjamin, New York).

Baroncelli, A., 1974, Nucl. Instrum. Methods 118, 445.

Benkheiri, P., *et al.*, 1977, Nuovo Cimento Lett. 20, 297.

Berman, S.M. and M. Jacob, 1965, Phys. Rev. 139, 1023.

Bricman, C., *et al.*, 1978, Phys. Lett. 75B.

Button - Shafer, J., 1965, Phys. Rev. 139, 607.

Eadie, W.T., *et al.*, 1971, *Statistical Methods in Experimental Physics* (North Holland, Amsterdam).

Eisenstein, B., *et al.*, 1978, Phys. Rev. D18, 1370.

Ferrer, A., *et al.*, 1978, Nucl. Phys. B142, 77.

Gottfried, K. and J.D. Jackson, 1964, Nuovo Cimento 33, 309.

Jackson, J.D., 1964, Nuovo Cimento 34, 1644.

Jones, W.V., 1969, Phys. Rev. 187, 1868.

Morris, G.R., 1975, Ph.D. Thesis, Univ. of Ill. (unpublished).

Ranft, J., 1972, Particle Accelerators 3, 129.

Scharre, D.L., *et al.*, 1978, Phys. Rev. D17, 2853.

Sokolsky, P., 1973, Ph.D. Thesis, Univ. of Ill. (unpublished).

Wagner, R.G., 1978, Ph.D. Thesis, Univ. of Ill. (unpublished).

[redacted]

[redacted] He received his elementary education at public and parochial schools in Syracuse, N.Y. and Franklin, Mass., graduating from Marian High School in Framingham, Mass. In 1970 he entered Cornell University from which he earned a B.S. degree in Applied and Engineering Physics in 1974. At the University of Illinois since 1974, the author took a M.S. degree in 1975 and has worked as a teaching assistant and research assistant in high energy physics. Publications to which he has contributed include, with B. Eisenstein, J. Elliott, W. Mollet, B. Nelson, D.S. Rhines, R.G. Wagner, J. Watson, N.M. Gelfand, and G.R. Morris, "Backward Resonance Production in $\pi^- p \to n\pi^+\pi^-$ at 8 GeV/c," Phys. Rev. D18, 1370 (1978), and, with A.L. Sessoms, M.S. Goodman, L. Holcomb, E.S. Sadowski, A. Strominger, B. Eisenstein, L.E. Holloway, S.C. Wright, and R.D. Kephart, "The Segmented Calorimeter: A Study of Hadron Shower Structure," Nucl. Instrum. Methods 161, 371 (1979).